J. Mech. Phys. Solids 181 (2023) 105470

Contents lists available at ScienceDirect

Journal of the Mechanics and Physics of Solids

journal homepage: www.elsevier.com/locate/jmps

Isogeometric smooth crack-band model (isCBM) using spress–sprain relations adapted to microplane theory

Hoang Nguyen [a], Weican Li [a], Zdeněk P. Bažant [b], Yuri Bazilevs [a,*]

[a] School of Engineering, Brown University, USA
[b] Department of Civil and Environmental Engineering, Northwestern University, USA

ARTICLE INFO

Keywords:
Quasibrittle fracture
Smooth crack band model
Isogeometric analysis
Softening damage
Localization limiter
Displacement curvature
Sprain tensor
Sprain-displacement matrix
Spress–sprain relations
Material characteristic length
Material rotation gradient

ABSTRACT

Recent optimum fitting of the data from eleven different types of distinctive fracture tests of quasibrittle materials, including the gap tests and the size effect tests, revealed that the crack band model (CBM) with the M7 damage constitutive law outperforms all the other existing computational fracture models for concrete. This is attributed to physically correct boundary conditions, especially those at the crack faces,to the crack front of finite width which allows using a triaxial tensorial damage constitutive law, and to choosing for this law a realistic material behavior description, the M7. Nevertheless the CBM has limitations—the width of the crack band cannot be varied, the statistically smooth damage distribution across the band cannot be resolved, and the propagation direction is biased by the mesh orientation when a regular mesh is used. These limitations have been overcome by the smooth crack band model (sCBM), which uses unconventional homogenization of damage mechanics to yield an additional Helmholtz free energy density, called the "sprain energy". This energy is a function of the *curvature* tensor (or a hessian) of the vectorial displacement field, called the "sprain curvature tensor" (or sprain tensor for brevity), which is a sum of the strain gradient tensor and, importantly, the rotation gradient tensor. But, in a previous study, difficulties arose in computational implementation—the use of constant-strain elements required the curvature to be resisted by sprain forces that represented the derivatives of sprain energy with respect to nodal displacements and had to be applied on the nodes of adjacent elements. The need for adjacent nodes is here avoided by a variational derivation of the Isogeometric Smooth Crack-Band Model (isCBM). The microplane damage constitutive model M7 for concrete is adopted, which is made possible by establishing the relations of the sprain stress (or spress, for brevity) and sprain on microplanes of arbitrary orientations. Using Isogeometric Analysis (IGA) based on non-uniform rational B-Splines (NURBS), the excessive displacement curvature and its resistance (spress) can be described by the shape functions with C^1-continuity. Computational results show that the orientation bias of regular meshes is eliminated while keeping the constitutive law intact, which is important for compatibility with the existing material laws in general. In addition, comparisons with experimental data reveal that isCBM with M7 can reproduce the correspondence between the size of the fracture process zone and the fracture energy, as indicated by gap tests. Finally, the isCBM does not compromise the strain-path-dependence of material response.

* Corresponding author.
E-mail address: yuri_bazilevs@brown.edu (Y. Bazilevs).

https://doi.org/10.1016/j.jmps.2023.105470
Received 18 July 2023; Received in revised form 19 September 2023; Accepted 14 October 2023
Available online 17 October 2023
0022-5096/© 2023 Elsevier Ltd. All rights reserved.

In honor of Huajian Gao, a great friend, supportive colleague, and a top applied mechanician of his generation, on the occasion of his 60th birthday.

Yuri Bazilevs and Zdeněk P. Bažant, speakers at the Workshop in honor of Gao.

1. Introduction

Finite element analysis of fracture began with Ray W. Clough's 1962 epoch-making assessment (Clough, 1962; Clough and Wilson, 1962) of the safety of cracked Norfolk Dam using over a hundred constant-strain triangular finite elements of a continuum that he derived variationally in 1960 (Clough, 1960). Yet, six decades later and thousands of papers published, the theory of computational fracture mechanics is still far from being complete.

Recent comparisons with eleven published distinctive types of fracture tests of quasibrittle materials important for practice, particularly with the gap test, the size effect tests and the shear fracture tests, revealed that the recently popular peridynamics and phase field models (Bažant et al., 2022) cannot fit the published data and show major discrepancies. Their fundamental hypotheses were also shown to be unrealistic. Besides, peridynamics as well as the classical nonlocal models give unphysical representation of boundary conditions, which is particularly problematic at near-tip crack surfaces and at fracture process zone (FPZ) interfaces. The crack band model (CBM) (Bažant and Oh, 1983; Bažant and Planas, 1998) was shown in Bažant and Nguyen (2023) to outperform the other methods and agree with all the data from the distinctive fracture tests.

In addition to correct boundary conditions, the main asset of CBM is the finite width of its fracture process zone (FPZ) allowing the use of a tensorial triaxial damage constitutive law, which must, of course, be realistic to achieve good performance. Nevertheless, there are limitations—(1) the width of the crack band cannot be varied, (2) the gradual, statistically smooth, variation of damage across the band cannot be resolved and, (3) the propagation direction is biased by the orientation of mesh lines if a regular (rather than random) mesh is used.

All three limitations were overcome by the smooth crack band model (sCBM), developed in 2022 by Zhang and Bažant (2023). The sCBM enforces nonlocality by limiting the curvature (characterizing the hessian) of the vectorial displacement field. This is achieved by an unorthodox material homogenization which shows that, for damage behavior, the Helmholtz free energy density of the material must consist not only of the strain energy, Ψ, as in classical continuum mechanics, but also of an additional energy density, Φ, called the sprain energy (the term "sprain" was co-opted from medicine where it refers to a ligament damage distributed over a finite length, as opposed to ligament rupture). Φ is a function of the "sprain tensor", defined as the tensor of curvature (or hessian, or second gradient) of the vectorial displacement field. The latter has the dimension of m^{-1} and is multiplied by the material characteristic length l_0 to become dimensionless. The resistance of the curvature development, or sprain, will force the variation of damage across the crack band to be gradual, almost smooth, hence the name of the method. It is important to note that the sprain tensor represents a sum of the strain gradient tensor and the rotation gradient tensor. The lack of the latter has been a limitation of the recent computational strain-gradient models, particularly in the case of shear damage and fracture.

The use of sCBM based on constant strain elements ran into computational difficulties. The derivatives of sprain energy with respect to nodal displacements provided self-equilibrated sets of forces, called the sprain forces (Zhang and Bažant, 2023), some of which had to be applied on the nodes of adjacent elements to resist excessive curvature (or sprain). However, implementing it in a commercial finite element (FE) code such as Abaqus was found to increase the running time by one to two orders of magnitude. To avoid it, it is obviously necessary to apply all the curvature resisting forces within one and the same finite element while ensuring continuity of the first displacement gradient across the finite element boundary. Unfortunately, the standard quadratic and cubic finite elements cannot satisfy this requirement. Therefore, we turn to the isogeometric analysis (IGA) in which full displacement gradient continuity is enabled by the non-uniform rational B-Splines (NURBS) (Hughes et al., 2005; Cottrell et al., 2009), whose knot spans and control points are designed to produce shape functions with C^1-continuity.

If adjacent nodes are not considered, the nodal sprain forces become undefinable. Rather, we need to introduce the derivative of the sprain energy density with respect to the sprain tensor. This derivative calls for a mechanical quantity that has a role similar to the stress tensor and is work-conjugate to the sprain (or displacement curvature). For brevity, we introduce for this quantity a new term—the *"spress"*, of dimension N/m, which is a higher-order counterpart of stress (dimension N/m^2), and has the same dimension as the surface tension or fracture energy. The spress may be regarded as the surface density of sprain energy.

While the material behavior on the level of first displacement gradient (i.e., the deformation tensor) is traditionally described by the stress–strain constitutive relations, the material behavior on the level of the second displacement gradient, or sprain, must be described by the *spress–sprain* constitutive relations. If a sprain potential exists, its derivatives provide the spress–sprain relation and the corresponding sprain stiffness tensor. In the previous work (Zhang and Bažant, 2023), the spress–sprain and stress–strain constitutive relations were implicitly considered as separate. In general, though, these relations are likely to be combined, which is what is considered here.

Adapting microplane model M7 for concrete to the spress–sprain relations is another challenging goal of this study.

The strain-field regularization approach proposed here may be clarified by the following physical observations. The inhomogeneities in quasi-brittle materials (Fig. 1a) are normally homogenized into a material point constitutive law based on local deformation (dashed line in Fig. 1a). In many cases, such homogenization suffices to capture the material behavior but, when the damage is localized, key information goes missing because the local field variation (solid line in Fig. 1a) is also important. For example, the coarse aggregate pieces of higher stiffness cause locally elevated strains and stresses with a certain minimal spacing of microcracks. Likewise, this microstructural behavior resists the relative rotations of adjacent aggregate pieces or of adjacent

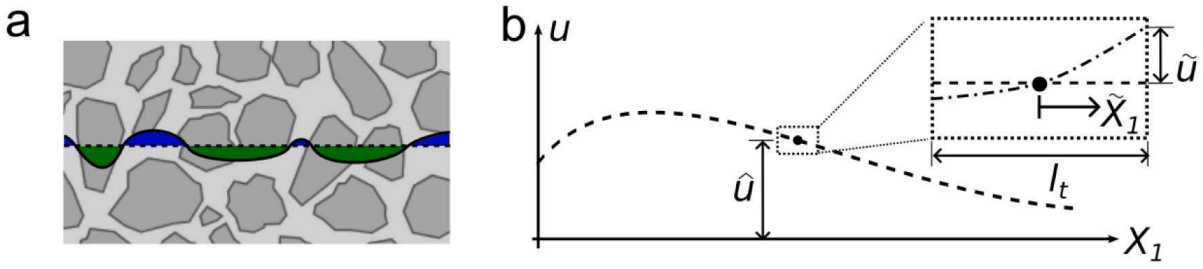

Fig. 1. (a) Local variation of the strain profile around a mean strain value is caused by the inhomogeneity within a mesoscopically homogeneous material; (b) 1D displacement of a material point within a microscale cell equals to the sum of the mean profile and local oscillations.

representative volumes of the material. This cannot be adequately captured by the classical equilibrium-based homogenization. Rather, as proposed in Zhang and Bažant (2023), it is the homogenization of energy that helps to explain the necessity of the aforementioned additional sprain energy, $\boldsymbol{\Phi}$.

Placing the isCBM into the broad context of quasibrittle fracture mechanics and its regularized computational modeling is postponed to Appendix H.

2. Microscale-mesoscale bridging

2.1. General formulation

We assume that a mesoscale cell of volume V_c contains a heterogeneous microscale structure (see Fig. 1b). A similar assumption was used in other theories, such as mechanism-based strain gradient plasticity (Hutchinson and Fleck, 1997), imbricate continuum (Bažant, 1984), and the variational multiscale method (Hughes et al., 1998).

The center of such mesoscale material cell has the coordinates $\boldsymbol{X}$ in the (undeformed) referential configuration. The location of a material point within this cell in the current configuration is

$$\boldsymbol{x} = \boldsymbol{X} + \hat{\boldsymbol{u}} + \tilde{\boldsymbol{u}} \tag{1}$$

Taking the gradient with respect to the referential coordinates yields

$$\boldsymbol{F} = \boldsymbol{I} + \boldsymbol{\nabla}\hat{\boldsymbol{u}} + \boldsymbol{\nabla}\tilde{\boldsymbol{u}}, \tag{2}$$

where $\boldsymbol{\nabla} = \boldsymbol{\nabla}_X$. The gradient with respect to the current configuration $\boldsymbol{\nabla}_x$, if it exists, will be explicitly stated. Here, $\hat{\boldsymbol{u}}$ is the displacement at the center of the mesoscale cell and $\tilde{\boldsymbol{u}}$ is the displacement of any microscale material point within that cell (see Figs. 1b, c).

The Green–Lagrange (GL) strain of a microscale material point can be computed as

$$\begin{aligned}\tilde{\boldsymbol{E}} =& \frac{1}{2}\left(\boldsymbol{F}^{\intercal}\cdot\boldsymbol{F}-\boldsymbol{I}\right) = \frac{1}{2}\left[(\boldsymbol{I}+\boldsymbol{\nabla}\hat{\boldsymbol{u}}+\boldsymbol{\nabla}\tilde{\boldsymbol{u}})^{\intercal}\cdot(\boldsymbol{I}+\boldsymbol{\nabla}\hat{\boldsymbol{u}}+\boldsymbol{\nabla}\tilde{\boldsymbol{u}})-\boldsymbol{I}\right]\\ =& \frac{1}{2}\left[(\boldsymbol{\nabla}\hat{\boldsymbol{u}})^{\intercal}+\boldsymbol{\nabla}\hat{\boldsymbol{u}}+(\boldsymbol{\nabla}\hat{\boldsymbol{u}})^{\intercal}\cdot\boldsymbol{\nabla}\hat{\boldsymbol{u}}\right]+\frac{1}{2}\left[(\boldsymbol{\nabla}\tilde{\boldsymbol{u}})^{\intercal}+\boldsymbol{\nabla}\tilde{\boldsymbol{u}}+(\boldsymbol{\nabla}\tilde{\boldsymbol{u}})^{\intercal}\cdot\boldsymbol{\nabla}\tilde{\boldsymbol{u}}\right]+\\ &\frac{1}{2}\left[(\boldsymbol{\nabla}\hat{\boldsymbol{u}})^{\intercal}\cdot\boldsymbol{\nabla}\tilde{\boldsymbol{u}}+(\boldsymbol{\nabla}\tilde{\boldsymbol{u}})^{\intercal}\cdot\boldsymbol{\nabla}\hat{\boldsymbol{u}}\right],\end{aligned} \tag{3}$$

where the mixed terms represent the interaction of the mean and microscale displacements.

We denote by $\tilde{X}$ the location of a micro-scale material point in the mesoscale cell (see Fig. 1b). While a higher-order theory could be derived by keeping the quadratic and higher-order terms, we take here a Taylor-series expansion at X keeping only the linear term. This gives

$$\tilde{\boldsymbol{u}} = \boldsymbol{\nabla}\hat{\boldsymbol{u}}\cdot\tilde{\boldsymbol{X}}. \tag{4}$$

Taking a gradient of the above expression yields

$$\boldsymbol{\nabla}\tilde{\boldsymbol{u}} = \partial_J\tilde{u}_i = \partial_J\left(\partial_K\hat{u}_i\tilde{X}_K\right) = \left(\partial_J\partial_K\hat{u}_i\right)\tilde{X}_K = \frac{\partial^2\hat{u}_i}{\partial X_J\partial X_K}\tilde{X}_K = \eta_{JKi}\tilde{X}_K \tag{5}$$

Note that the $\tilde{X}_K$ is treated as a constant because the microscale material points share the same mesoscale coordinates with the center point of mesoscale cell. Here, η_{JKi} is the (J,K) component of the Hessian of the displacement vector. A symmetric permutation $\eta_{JKi} = \eta_{KJi}$ is applied to enforce the symmetry of mixed partial derivatives.

Rewriting Eq. (3) using index notation yields

$$\tilde{E}_{IJ} = \hat{E}_{IJ} + \frac{1}{2}\left(\eta_{IKJ}\tilde{X}_K + \eta_{JKI}\tilde{X}_K + \eta_{PRI}\eta_{PQJ}\tilde{X}_R\tilde{X}_Q\right) + \frac{1}{2}\left(\partial_I\hat{u}_i\eta_{JKi}\tilde{X}_K + \partial_J\hat{u}_i\eta_{IKi}\tilde{X}_K,\right) \tag{6}$$

where $\hat{E}_{IJ} = \frac{1}{2}(\partial_I \hat{u}_J + \partial_J \hat{u}_I + \partial_I \hat{u}_K \partial_J \hat{u}_K)$ is the mean-field GL strain. Eliminating the higher-order terms in Eq. (6) results in

$$\tilde{E}_{IJ} = \hat{E}_{IJ} + \frac{1}{2}\left(\eta_{JKi}\hat{F}_{iI} + \eta_{IKi}\hat{F}_{iJ}\right)\tilde{X}_K = \hat{E}_{IJ} + \hat{\Xi}_{IJK}\tilde{X}_K, \tag{7}$$

where

$$\hat{\Xi}_{IJK} = \frac{1}{2}\left(\eta_{JKi}\hat{F}_{iI} + \eta_{IKi}\hat{F}_{iJ}\right). \tag{8}$$

With the current index notation convention, the symmetry of $\boldsymbol{\Xi}$ is similar to that of $\boldsymbol{\eta}$, i.e., $\hat{\Xi}_{IJK} = \hat{\Xi}_{JIK}$. Note that the lower-case index in Eqs. (5) and (7) represents the displacement. From this point on, the "hat" notation will be dropped to simplify the presentation.

We denote the second Piola–Kirchhoff (PK2) stress by $\tilde{\boldsymbol{S}}$ and invoke the principle of virtual work over a mesoscale cell as follows:

$$\int_{V_c} \tilde{S}_{IJ}\delta\tilde{E}_{IJ}\mathrm{d}V = \int_{V_c} \tilde{S}_{IJ}(\delta E_{IJ} + \delta\Xi_{IJK}\tilde{X}_K)\mathrm{d}V. \tag{9}$$

Recognizing that in the above equation the variations $\delta\boldsymbol{E}$ and $\delta\boldsymbol{\Xi}$ are constant over a mesoscale cell, we obtain

$$\int_{V_c} \tilde{S}_{IJ}\delta\tilde{E}_{IJ}\mathrm{d}V = \left(S_{IJ}\delta E_{IJ} + T_{IJK}\delta\Xi_{IJK}\right)V_c, \tag{10}$$

where the stress resultants $\boldsymbol{S}$ and $\boldsymbol{T}$ are given by

$$\boxed{S_{IJ} = \frac{1}{V_c}\int_{V_c} \tilde{S}_{IJ}\mathrm{d}V} \tag{11}$$

$$\boxed{T_{IJK} = \frac{1}{V_c}\int_{V_c} \tilde{S}_{IJ}\tilde{X}_K\mathrm{d}V} \tag{12}$$

Updating the notation used in Zhang and Bažant (2023), we use $\boldsymbol{\Xi}$ for the *sprain* (or sprain curvature) tensor and $\boldsymbol{T}$ for the *spress* (or spress tensor, or sprain energy gradient tensor). Note the symmetry of $\boldsymbol{S}$ and $\boldsymbol{T}$, namely, $S_{IJ} = S_{JI}$ and $T_{IJK} = T_{JIK}$, which is the same as that of $\boldsymbol{E}$ and $\boldsymbol{\Xi}$, respectively.

The same procedure can be repeated to define the spress–sprain tensors corresponding to the microscale PK1 stress $\tilde{\boldsymbol{P}}$ and the deformation gradient $\tilde{\boldsymbol{F}}$, which we call $\boldsymbol{Q}$ and $\boldsymbol{\eta}$). Obviously, they are also work-conjugate quantities. The derivation of Q_{IJK} from $S_{IJ}, E_{IJ}, T_{IJK}, \Xi_{IJK}$, and η_{IJK} is presented in Appendix A.

2.2. Linearized small-strain version

For a linearized theory, the mesoscale–microscale relation may be rewritten as

$$\tilde{\varepsilon}_{IJ} = \varepsilon_{IJ} + \frac{1}{2}\left(\eta_{IKJ} + \eta_{JKI}\right)\tilde{X}_K = \varepsilon_{IJ} + \xi_{IJK}\tilde{X}_K; \varepsilon_{IJ} = \frac{1}{2}\left(\partial_I u_J + \partial_J u_I\right). \tag{13}$$

Applying the principle of virtual work over a mesoscale cell gives

$$\int_{V_c} \tilde{\sigma}_{IJ}\delta\tilde{\varepsilon}_{IJ}\mathrm{d}V = \left(\sigma_{IJ}\varepsilon_{IJ} + \tau_{IJK}\delta\xi_{IJK}\right)V_c, \tag{14}$$

where the stress resultants are given by

$$\boxed{\sigma_{IJ} = \frac{1}{V_c}\int_{V_c} \tilde{\sigma}_{IJ}\mathrm{d}V} \tag{15}$$

$$\boxed{\tau_{IJK} = \frac{1}{V_c}\int_{V_c} \tilde{\sigma}_{IJ}\tilde{X}_K\mathrm{d}V} \tag{16}$$

3. Governing equations of mechanical equilibrium

3.1. Small-strain version

The virtual work within volume V (here one needs to distinguish V as the domain volume from the mesoscale cell volume V_c) can be written in terms of the variation of the gradient, and the hessian of a virtual displacement $\delta\boldsymbol{u}$. We have

$$\int_V \left(\sigma_{IJ}\partial_J\delta u_I + \tau_{IJK}\partial_J\partial_K\delta u_I\right)\mathrm{d}V = \int_S n_J\left(\sigma_{IJ} - \partial_K\tau_{IKJ}\right)\delta u_I dS + \int_S \left[n_J\tau_{IJK}\left(\partial_K\delta u_I\right)\right]dS$$
$$- \int_V \left(\partial_J\sigma_{IJ} - \partial_K\partial_J\tau_{IJK}\right)\delta u_I\mathrm{d}V. \tag{17}$$

In Eq. (17), the divergence theorem has been applied. Here note that δu_I and $\partial_K \delta u_I$ are not independent. Therefore, it is necessary to decompose $\partial_K \delta u_I$ into the surface and normal gradients. The normal gradient is given by

$$\partial^n = n_J \partial_J, \tag{18}$$

while the surface gradient by

$$\partial^s_K = \partial_K - n_K n_J \partial_J = \delta_{JK}\partial_J - n_K n_J \partial_J = (\delta_{JK} - n_K n_J)\partial_J. \tag{19}$$

The second term on the RHS of Eq. (17) yields

$$\begin{aligned} &\int_S \left[n_J \tau_{IJK} \left(\partial^s_K + n_K \partial^n \right) \delta u_I \right] dS \\ &= \int_S \left(n_J n_K \tau_{IJK} \right) \partial^n \delta u_I dS + \int_S \left(\partial^s_i n_i \right) n_K n_J \tau_{IJK} \delta u_I dS - \int_S \partial^s_K \left(n_J \tau_{IJK} \right) \delta u_I dS \end{aligned} \tag{20}$$

In the last equation, the surface divergence theorem has been applied, i.e.,

$$\int_S \partial^s_I \left(\Phi_{IJ} v_J \right) dS = \int_S \left(\partial^s_i n_i \right) n_I \Phi_{IJ} v_J dS \tag{21}$$

Therefore, the displacement field needs to satisfy one governing equation and two natural boundary conditions so that the internal and external virtual work would be in balance, i.e., $\int_S r_I \partial^n \delta u_I dS + \int_S t_I \delta u_I dS - \int_V f_I \delta u_I \mathrm{d}V = \delta W_{\text{ext}},\ \forall \delta u_I$. This implies,

$$f_I = \partial_J \left(\sigma_{IJ} - \partial_K \tau_{IJK} \right) + b_I = \rho \ddot{u}_I \text{ on } \Omega \tag{22}$$

$$t_I = n_J \left(\sigma_{IJ} - \partial_K \tau_{IKJ} \right) + n_J \left(\partial^s_i n_i \right) n_K \tau_{IJK} - \partial^s_K \left(n_J \tau_{IJK} \right) = t^{\text{ext}}_I \text{ on } (\partial\Omega)_t \tag{23}$$

$$r_I = n_J n_K \tau_{IJK} = r^{\text{ext}}_I \text{ on } (\partial\Omega)_r \tag{24}$$

where b_I and $\rho \ddot{u}_I$ arise as the body and inertia force terms.

3.2. Finite-strain version

Following the same procedure, one can write the mechanical equilibrium conditions for the large-deformation case:

$$f_I = \partial_J \left(P_{IJ} - \partial_K Q_{JKI} \right) + b_I = \rho \ddot{u}_I \text{ in } \Omega, \tag{25}$$

$$t_I = n_J \left(P_{IJ} - \partial_K Q_{KIJ} \right) + \left(\partial^s_i n_i \right) n_J n_K Q_{JKI} - \partial^s_K \left(n_J Q_{JKI} \right) = t^{\text{ext}}_I \text{ on } (\partial\Omega)_t, \tag{26}$$

$$r_I = n_J n_K Q_{JKI} = r^{\text{ext}}_I \text{ on } (\partial\Omega)_r, \tag{27}$$

Here P_{IJ} is the first Piola–Kirchhoff (PK1) stress (or the transpose of the nominal stress). Other terms were explained in the previous section.

4. Constitutive modeling

4.1. Two simple hypotheses for introducing the sprain into damage constitutive law

Finding the optimal and most realistic way of combining the strain and sprain in the constitutive law is a challenge made difficult by lack of experimental data and micro-mechanical theory for test specimens subjected to the second displacement gradient. Lacking such data, we have two simple choices:

- Separate sprain constitutive law
- Sprain incorporated into an existing constitutive law

In this study, we focus on the latter approach.

4.2. Constitutive laws for spress–sprain relation

In this section, the relation of spress to the sprain deformation or, in short, the spress–sprain relation, is derived and compared with the conventional strain–stress law in the microscale cell. We start with the most simplified damage law—Mazars' scalar continuum damage model, even though its practical applicability is rather limited. Then we extend the modeling to a more realistic case—the M7 microplane damage model.

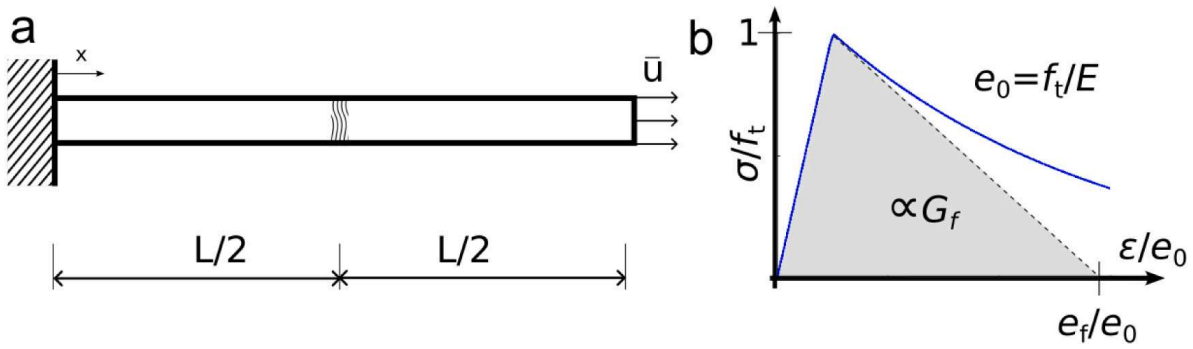

Fig. 2. (a) A one-dimensional bar containing a weak material point at the middle of its length is subjected to uniaxial tension; (b) A 1D illustration of the constitutive law described in Eqs. (29)–(33).

4.2.1. Mazars' scalar damage model

Mazars (1984) and Pijaudier-Cabot and Mazars (2001) proposed a damage model based on the Helmholtz free energy that is released through a damage variable ω,

$$f(\boldsymbol{E},\omega) = \frac{1}{2}\boldsymbol{E}_e : \boldsymbol{D}_e : \boldsymbol{E}_e = \frac{1}{2}(1-\omega)^2 \boldsymbol{E} : \boldsymbol{D}_e : \boldsymbol{E}, \tag{28}$$

where $\boldsymbol{D}_e$ is the elastic stiffness tensor of the pristine material and $\boldsymbol{E}_e$ is the "intact" strain. Despite its limitations, e.g., the inability to represent the effect of crack parallel stresses or shear loads, this simple damage constitutive model will suffice for demonstration purposes.

The PK2 stress and thermodynamic force Y (the quantity conjugate by work to the damage variable ω) are calculated as

$$\boldsymbol{S} = \frac{\partial f}{\partial \boldsymbol{E}} = (1-\omega)^2 \boldsymbol{D}_e : \boldsymbol{E} \tag{29}$$

$$Y = -\frac{\partial f}{\partial \omega} = (1-\omega)\boldsymbol{E} : \boldsymbol{D}_e : \boldsymbol{E} \tag{30}$$

The damage potential, which characterizes the relation between the change of the damage variable and that of total strain E_{ij} is chosen as

$$\omega = 1 - \sqrt{\frac{e_0}{\zeta}\left[\exp\left(-\frac{\zeta - e_0}{e_f - e_0}\right)\right]} \tag{31}$$

$$\zeta = \max_{\text{loading history}}(\bar{\chi}) \tag{32}$$

$$\bar{\chi} = \sqrt{\sum_{k=1,\text{dim}} \langle \chi_k \rangle : \langle \chi_k \rangle}, \tag{33}$$

where χ_k is the kth-eigenvalue of $\boldsymbol{E}$. In this model, the microcracks are assumed to rotate, aligning always with the principal strain directions. Also, only the positive parts of principal strains are considered, which is expressed by applying the Macaulay brackets $\langle\ \rangle$ to the principal strains. The damage initiation strain is $e_0 = f_t/E$, where E is the Young's modulus and f_t is the cohesive strength. The fracture strain is calculated via

$$e_f = g_f/f_t + e_0 \tag{34}$$

where g_f is the apparent energy dissipated by one material point (energy per unit volume, see Fig. 2b). The apparent fracture strain e_f is, therefore, not the strain where the cohesive stress reduces to zero, but the intersection between the initial softening slope with the horizontal axis. Hoover and Bažant (2014) pointed out that this value, g_f, would be directly related to the initial fracture energy G_f and the total fracture energy G_F of the material. Hoover and Bažant (2014) also indicated that while the former dominates the load capacity of structures while the latter is essential where energy dissipation matters, as in projectile penetration. In this light, the initial fracture energy of the material is computed as $G_f = 0.5 g_f w_{\text{char}}$, where $0.5 g_f$ is the area of the triangle shown in Fig. 2b and w_{char} is a size (usually referred to as characteristic size) that captures the extent of the damage zone. The quantity w_{char} plays the role of a localization limiter.

4.2.2. Derivation from a constitutive model

As the coordinate origin of $\tilde{X}_k$ is located at the centroid of the cell, the following equations hold:

$$\frac{1}{V_c}\int_{V_c} \mathrm{d}V = 1;\ \int_{V_c} \tilde{X}_k \mathrm{d}V = 0;\ \frac{1}{V_c}\int_{V_c} \tilde{X}_k \tilde{X}_m \mathrm{d}V = \frac{l_t^2}{12}\delta_{km}, \tag{35}$$

where l_t is the size of the mesoscale cell.

Variation of a physical quantity within a mesoscale cell can be approximated via a Taylor series expansion as

$$\tilde{p}(\tilde{\boldsymbol{X}}) = \tilde{p}|_{\tilde{\boldsymbol{X}}=\boldsymbol{0}} + \frac{\partial \tilde{p}}{\partial \tilde{\boldsymbol{X}}}\Big|_{\tilde{\boldsymbol{X}}=\boldsymbol{0}} \tilde{\boldsymbol{X}} + \mathcal{O}(\tilde{\boldsymbol{X}}^2) \tag{36}$$

and, if such a quantity is homogeneous of order 1 with respect to $\tilde{X}_k$ (i.e., $f(\lambda\tilde{X}) = \lambda f(\tilde{X})$), the expression simplifies to

$$\frac{\partial \tilde{p}}{\partial \tilde{\boldsymbol{X}}} \tilde{\boldsymbol{X}} = \tilde{p} \tag{37}$$

Implicitly, we assume that the mesoscale cell size l_t is smaller than the relevant structure size or the ligament length in the notched specimens.

Owing to the explicit form of Mazars-Pijaudier's constitutive law, the stress average may be computed as

$$S_{IJ} = \frac{1}{V_c}\int_{V_c} \tilde{S}_{IJ}\mathrm{d}V = (1-\omega)^2 (D_e)_{IJKL} : (E)_{KL} \tag{38}$$

The spress, on the other hand, becomes

$$\begin{aligned} T_{IJK} &= \frac{1}{V_c}\int_{V_c} \tilde{S}_{IJ}\tilde{X}_K \mathrm{d}V \\ &= \frac{l_t^2}{12}\left[(1-\omega)^2 (D_e)_{IJPQ}\delta_{KR} - 2(1-\omega)\frac{\partial \omega}{\partial E_{PQ}}(D_e)_{IJLM}(E)_{LM}\delta_{KR}\right]\Xi_{PQR}, \end{aligned} \tag{39}$$

where

$$\frac{\partial \omega}{\partial E_{IJ}} = \frac{\left[\frac{e_0}{\zeta^2} + \frac{e_0}{\zeta(e_f - e_0)}\right]}{2\sqrt{\frac{e_0}{\zeta}\exp\left(-\frac{\zeta - e_0}{e_f - e_0}\right)}} \exp\left(-\frac{\zeta - e_0}{e_f - e_0}\right) \sum_{k=1}^{dim} \frac{\langle \lambda_k \rangle \mathcal{H}(\lambda_k)}{\bar{\lambda}} \left[(N_k)_I (N_k)_J\right] \tag{40}$$

Here $\mathcal{H}$ is the Heaviside step function and N_k is the eigenvector corresponding to the kth eigenvalue of the stretch tensor $\boldsymbol{U}$.

One may wish to simplify the form of the spress in Eq. (39). For this, the following observations may be used:

- The sixth-order tensor that relates the T_{IJK} and Ξ_{IJK} can be computed from the fourth-order elastic tensor and damage coefficient.
- Another noteworthy feature of the sixth-order tensor is the separation of δ_{KR} from the remaining terms, this means that the resistance only appears in the direction where the higher-order derivative is taken.
- The growth rate of damage in this sixth-order tensor is slower than that of the fourth-order tensor due to the emergence of the lower order term $1-\omega$.

From these observations, we suggest the following form of the spress tensor:

$$T_{IJK} = \frac{l_t^2}{12}(1-\omega)^{\beta}\mathbb{D}_{IJKPQR}\Xi_{PQR}, \tag{41}$$

where $\mathbb{D}_{IJKPQR} = (D_e)_{IJPQ}\delta_{KR}$ is the sixth-order elastic tensor. The term $(1-\omega)^{\beta}$ is used instead of $(1-\omega)$ to take into account the averaged nature of this approximation and $\beta < 2$ makes sure that the damage driving T_{IJK} is growing slower than the one driving S_{IJ}.

4.2.3. Comparing the spress–sprain law to a general spherical–deviatoric decomposition of isotropic third-order tensors

Following Monchiet and Bonnet (2011), any third-order tensor having the symmetry property $\Xi_{IJK} = \Xi_{JIK}$ can be decomposed as

$$\boldsymbol{\Xi} = \boldsymbol{\Xi}_{d1} + \boldsymbol{\Xi}_{d2} + \boldsymbol{\Xi}_{v1} + \boldsymbol{\Xi}_{v2} \tag{42}$$

Note that this form is a generalized version of the SFH decomposition (Gurtin and Anand, 2005a,b). The spherical (volumetric) and deviatoric parts of $\boldsymbol{\Xi}$ may be written as

$$\left(\boldsymbol{\Xi}_{v1}\right)_{IJK} = \frac{1}{5}\left(2\Xi_{iiK} - \Xi_{Kii}\right)\delta_{IJ}, \tag{43}$$

$$\left(\boldsymbol{\Xi}_{v2}\right)_{IJK} = \frac{1}{10}\left(3\Xi_{Iii} - \Xi_{iiI}\right)\delta_{JK} + \frac{1}{10}\left(3\Xi_{Jii} - \Xi_{iiJ}\right)\delta_{IK} \tag{44}$$

and

$$\begin{aligned} \left(\boldsymbol{\Xi}_{d1}\right)_{IJK} &= \frac{1}{3}\left(\Xi_{IJK} + \Xi_{IKJ} + \Xi_{JKI}\right) - \frac{1}{15}\Big[\left(\Xi_{iiK} + 2\Xi_{Kii}\right)\delta_{IJ} + \left(\Xi_{iiI} + 2\Xi_{Iii}\right)\delta_{JK} \\ &+ \left(\Xi_{iiJ} + 2\Xi_{Jii}\right)\delta_{IK}\Big] \end{aligned} \tag{45}$$

$$\begin{aligned} \left(\boldsymbol{\Xi}_{d2}\right)_{IJK} &= \frac{1}{3}\left(2\Xi_{IJK} - \Xi_{IKJ} - \Xi_{JKI}\right) - \frac{1}{30}\Big[\left(10\Xi_{iiK} - 10\Xi_{Kii}\right)\delta_{IJ} \\ &+ \left(4\Xi_{Iii} - 3\Xi_{iiI}\right)\delta_{JK} + \left(4\Xi_{Jii} - 3\Xi_{iiJ}\right)\delta_{IK}\Big], \end{aligned} \tag{46}$$

respectively. These tensors are mutually orthogonal, that is, $\boldsymbol{\Xi}_{vm} : \boldsymbol{\Xi}_{dn} = 0$ and $\boldsymbol{\Xi}_{vm} : \boldsymbol{\Xi}_{vn} = 0$, $\boldsymbol{\Xi}_{dm} : \boldsymbol{\Xi}_{dm} = 0$, $\forall m \neq n$. The quadratic invariants are then formed by taking norms of these tensors.

For the constitutive law to be objective, it should be formulated in terms of these invariants via a sixth-order tensor. Here, we consider the isotropic case only. According to Monchiet and Bonnet (2011), any sixth-order isotropic tensor can be expressed as a linear combination of six independent terms:

$$\mathbb{T} = \tilde{\lambda}_1 \mathbb{J}_1 + \tilde{\lambda}_2 \mathbb{J}_2 + \tilde{\lambda}_3 \mathbb{J}_3 + \tilde{\lambda}_4 \mathbb{J}_4 + \tilde{\mu}_1 \mathbb{K}_1 + \tilde{\mu}_2 \mathbb{K}_2, \tag{47}$$

with

$$\mathbb{J}_1 = \frac{1}{5}\left(2\mathbb{T}_1 - \mathbb{T}_4\right), \tag{48}$$

$$\mathbb{J}_2 = \frac{1}{5}\left(3\mathbb{T}_4 - \mathbb{T}_1\right), \tag{49}$$

$$\mathbb{J}_3 = \frac{1}{5}\left(2\mathbb{T}_3 - \mathbb{T}_6\right), \tag{50}$$

$$\mathbb{J}_4 = \frac{1}{5}\left(3\mathbb{T}_6 - \mathbb{T}_3\right), \tag{51}$$

$$\mathbb{K}_1 = \frac{1}{3}\left(\mathbb{T}_2 + 2\mathbb{T}_5\right) - \frac{1}{15}\left(\mathbb{T}_1 + 2\mathbb{T}_4\right) - \frac{2}{15}\left(\mathbb{T}_3 + 2\mathbb{T}_6\right), \tag{52}$$

$$\mathbb{K}_2 = \frac{2}{3}\left(\mathbb{T}_2 - \mathbb{T}_5\right) + \frac{1}{3}\left(\mathbb{T}_4 - \mathbb{T}_1 + \mathbb{T}_3 - \mathbb{T}_6\right), \tag{53}$$

where the $\mathbb{T}$-terms can be found in Appendix B. We note that $\mathbb{J}_1$–$\mathbb{J}_4$ terms represent the volumetric and $\mathbb{K}_1 - \mathbb{K}_2$ the deviatoric parts, respectively. The spress–sprain constitutive law may be expressed in a general form as

$$\boldsymbol{T} = \mathbb{T} : \boldsymbol{\Xi}. \tag{54}$$

We can now rewrite Eq. (41) as follows:

$$T_{IJK} = (1-\omega)^{\beta} \frac{l_t^2}{12}\left[\lambda \delta_{IJ}\delta_{PQ} + \mu(\delta_{IP}\delta_{JQ} + \delta_{IQ}\delta_{JP})\right]\delta_{KR}\Xi_{PQR} \tag{55}$$

From Appendix B, we can see that only $\mathbb{T}_1$ and $\mathbb{T}_2$ appear in Eq. (55). While $\mathbb{T}_1$ is present in both the volumetric and deviatoric parts, $\mathbb{T}_2$ only appears in the latter. The independent material constants in Eq. (47) can now be expressed as follows:

$$\tilde{\lambda}_1 = (1-\omega)^{\beta}\frac{l_t^2}{12}(3\lambda + 2\mu);\ \tilde{\lambda}_2 = (1-\omega)^{\beta}\frac{l_t^2}{12}\lambda;\ \tilde{\lambda}_3 = 0;\ \tilde{\lambda}_4 = \tilde{\mu}_1 = \tilde{\mu}_2 = (1-\omega)^{\beta}\frac{l_t^2}{12}2\mu \tag{56}$$

These relations come from the solution of the linear system of equations shown in Appendix B. Note that, in the metric system, the units of $\tilde{\mu}$ and $\tilde{\lambda}$ are Pa-m^2, suggesting a length scale over which the spress will take effect.

4.2.4. Separation of shear and tensile regularization length scales

From Eq. (55), we can take advantage of the fact that $\mathbb{T}_2$ only appears in the deviatoric part of $\mathbb{T}$ to differentiate the regularization of opening and shear crack width. By applying different length scales to the corresponding terms controlling these mechanisms, we obtain

$$T_{IJK} = \left[(1-\omega_t)^{\beta}\frac{l_t^2}{12}\lambda\delta_{IJ}\delta_{PQ} + (1-\omega_s)^{\beta}\frac{l_s^2}{12}\mu(\delta_{IP}\delta_{JQ} + \delta_{IQ}\delta_{JP})\right]\delta_{KR}\Xi_{PQR}, \tag{57}$$

where ω_t, ω_s are the variables controlling the tensile and shear damage. The effective damage may be computed as $\omega = 1 - (1-\omega_t)(1-\omega_s)$ in this case

4.3. Coupling of the strain and sprain deformation tensors

To further prevent localization, one can define an equivalent strain with contributions from both $\boldsymbol{E}$ and $\boldsymbol{\Xi}$. Using Mazars' scalar damage model as an example, the resistance against stretching parameter may be defined as

$$\bar{\chi} = \sqrt{\sum_{i=I}^{III}\langle\chi_i\rangle^2} + w_t\sqrt{\boldsymbol{\Xi}_v : \boldsymbol{\Xi}_v} \tag{58}$$

or, more generally, as

$$\bar{\chi} = f(\chi) + w_t\left\langle\sqrt{\boldsymbol{\Xi}_v : \boldsymbol{\Xi}_v} - C\right\rangle \tag{59}$$

Here, C is chosen by the user and its value depends on the level of noise in the discrete model. To distinguish between the volumetric and deviatoric damage, the following form could be used:

$$\bar{\chi} = f(\chi) + w_t\left\langle\sqrt{\boldsymbol{\Xi}_v : \boldsymbol{\Xi}_v} - C_t\right\rangle + w_s\left\langle\sqrt{\boldsymbol{\Xi}_d : \boldsymbol{\Xi}_d} - C_s\right\rangle \tag{60}$$

As is evident from Eqs. (39) and (58), both l_t and w_t (or w_s and l_s in the case of a shear crack) contribute to the strain regularization. While the former controls the coupling between sprain and spress, the latter relates the strain and sprain tensors. A parametric study presented later in the paper will reveal the effects and relative importance of each term.

Up to now, there emerge four length-scale parameters, l_t, w_t, l_s, w_s that control the localization behavior in the opening and shear cracks. Constraints such as $l_s/w_s = l_t/w_t$ or $l_s = l_t$ may be applied in order to avoid model overfitting.

4.4. Adaptation to a vectorial form of the constitutive law—microplane model M7

Usually, stress–strain constitutive laws are formulated for a stress tensor where the strain tensor or its increment are used as input. However, such laws can also be derived from the vectorial projections of these tensors on the so-called microplanes, representing planes of various discrete orientations that may be imagined as facets whose normals represent numerical integration points on a spherical surface centered at the continuum point (Bažant and Oh, 1985; Bažant and Planas, 1998; Bažant et al., 2021). In this work, we use the M7 version of the microplane model for concrete. Both the general description of the microplane theory and specific formulations for the M7 model can be found in Caner and Bažant (2013a,b) and Nguyen et al. (2021a) and are also provided in Appendix C.

To regularize the problem of cracking, we consider the microplane strain vector on a generic microplane and decompose it into the normal and tangential vectors (Fig. Appendix-1c). These vectors are the projection of the continuum strain tensor onto the microplanes, and we further decompose them into the microplane normal and tangential strain vector components (Bažant and Oh, 1985). For the normal component, defined by unit normal vector $\boldsymbol{n}$, we obtain:

$$\tilde{E}_{IJ} n_I n_J = E_{IJ} n_I n_J + n_I n_J \Xi_{IJK} \tilde{X}_K \tag{61}$$

The position vector can be decomposed into normal and tangential components as:

$$\tilde{X}_K = (\|\tilde{\boldsymbol{X}}\|_N n_K + \|\tilde{\boldsymbol{X}}\|_L l_K + \|\tilde{\boldsymbol{X}}\|_M m_K). \tag{62}$$

where l and m are orthogonal unit vectors in two suitably chosen orthogonal in-plane directions L and M (Bažant and Oh, 1985). $\|\tilde{\boldsymbol{X}}\|_N$, $\|\tilde{\boldsymbol{X}}\|_L$, $\|\tilde{\boldsymbol{X}}\|_M$ are projections of $\tilde{X}$ on N, L, M directions. Therefore, if we only focus on the variation of $\tilde{E}$ along the normal directions, following terms will remain:

$$\Xi_N = \mathcal{N}_{IJK} \Xi_{IJK}. \tag{63}$$

Similarly,

$$\Xi_L = \mathcal{L}_{IJK} \Xi_{IJK}, \tag{64}$$

$$\Xi_M = \mathcal{M}_{IJK} \Xi_{IJK}, \tag{65}$$

where

$$\mathcal{N}_{IJK} = n_I n_J n_K; \mathcal{L}_{IJK} = \frac{1}{2} n_K (l_I n_J + l_J n_I); \mathcal{M}_{IJK} = \frac{1}{2} n_K (m_I n_J + m_J n_I). \tag{66}$$

Note that, Ξ_N, Ξ_L, Ξ_M represents the variation of normal and tangential components of the microplane sprain deformation vector along the normal direction; see Fig. Appendix-1c. A complete set of terms should include:

$$\mathcal{N}^t_{IJK} = n_I n_J (l_K + m_K), \tag{67}$$

$$\mathcal{L}^t_{IJK} = \frac{1}{2} (l_K + m_K)(l_I n_J + l_J n_I), \tag{68}$$

$$\mathcal{M}^t_{IJK} = \frac{1}{2} (l_K + m_K)(m_I n_J + m_J n_I). \tag{69}$$

The microplane stresses can therefore be written in terms of the equivalent microplane strains instead of the conventional ones as

$$S_N = S_N(\bar{E}_N, \bar{E}_L, \bar{E}_M); S_L = S_L(\bar{E}_N, \bar{E}_L, \bar{E}_M); S_M = S_M(\bar{E}_N, \bar{E}_L, \bar{E}_M), \tag{70}$$

with the following definitions of the equivalent normal and tangential microplane strains:

$$\bar{E}_N = E_N + w_t \langle \left| \mathcal{N}_{IJK} \Xi_{IJK} \right| - C_N \rangle, \tag{71}$$

$$\bar{E}_M = E_M + w_s \langle \left| \mathcal{M}_{IJK} \Xi_{IJK} \right| - C_S \rangle, \tag{72}$$

$$\bar{E}_L = E_L + w_s \langle \left| \mathcal{L}_{IJK} \Xi_{IJK} \right| - C_S \rangle. \tag{73}$$

The increment of the microplane-projected second-order stress is now given by

$$\Delta S_N = \frac{\partial S_N}{\partial \bar{E}_N} \left(\Delta E_N + w_t \Delta \langle \left| \Xi_N \right| - C_N \rangle \right), \tag{74}$$

$$\Delta S_L = \frac{\partial S_L}{\partial \bar{E}_N} \left(\Delta E_N + w_t \Delta \langle \left| \Xi_N \right| - C_N \rangle \right)$$

$$+\frac{\partial S_L}{\partial \bar{E}_L}\left(\Delta E_L + w_s \Delta\langle\left|\Xi_L\right| - C_T\rangle\right) + \frac{\partial S_L}{\partial \bar{E}_M}\left(\Delta E_M + w_s \Delta\langle\left|\Xi_M\right| - C_T\rangle\right), \tag{75}$$

$$\Delta S_M = \frac{\partial S_M}{\partial \bar{E}_N}\left(\Delta E_N + w_t \Delta\langle\left|\Xi_N\right| - C_N\rangle\right) + \frac{\partial S_M}{\partial \bar{E}_L}\left(\Delta E_L + w_s \Delta\langle\left|\Xi_L\right| - C_T\rangle\right) + \frac{\partial S_M}{\partial \bar{E}_M}\left(\Delta E_M + w_s \Delta\langle\left|\Xi_M\right| - C_T\rangle\right), \tag{76}$$

where the explicit expressions for the tangent moduli were derived in Nguyen et al. (2021a).

On each microplane, the spress–sprain relation may be expressed as

$$T_N = \frac{l_t^2}{12}\mathcal{E}_N \Xi_N, \tag{77}$$

$$T_L = \frac{l_s^2}{12}\mathcal{E}_T \Xi_L, \tag{78}$$

$$T_M = \frac{l_s^2}{12}\mathcal{E}_T \Xi_M. \tag{79}$$

Note that the microplane spresses are decoupled, and $\mathcal{E}_N, \mathcal{E}_T$ are the deformation-dependent secant microplane moduli. For an elastic material in a pristine state these are given by

$$\mathcal{E}_N = \mathcal{E}_{N0} = \frac{E}{1-2\nu}, \tag{80}$$

$$\mathcal{E}_T = \mathcal{E}_{T0} = \frac{E(1-4\nu)}{(1-2\nu)(1+\nu)}. \tag{81}$$

The principle of virtual work for the spress is employed to convert the vectorial representation of the microplane model to the tensorial one used in the governing equations of mechanical equilibrium. For this, we write

$$T_{IJK}\delta\Xi_{IJK} = \frac{3}{2\pi}\oint_S (T_N\delta\Xi_N + T_L\delta\Xi_L + T_M\delta\Xi_M)\,\mathrm{d}S = \frac{3}{2\pi}\oint_S (\mathcal{N}_{IJK}T_N + \mathcal{L}_{IJK}T_L + \mathcal{M}_{IJK}T_M)\,\mathrm{d}S\ \delta\Xi_{IJK}, \tag{82}$$

which implies

$$T_{IJK} = \frac{3}{2\pi}\oint_S (\mathcal{N}_{IJK}T_N + \mathcal{L}_{IJK}T_L + \mathcal{M}_{IJK}T_M)\,\mathrm{d}S. \tag{83}$$

In the above equations, $\oint_S$ is the integral over a unit hemisphere. It is approximated according to the optimal Gaussian integration formula for a spherical surface (Bažant and Oh, 1986).

Remark 1. It can be seen from Appendix D that the sixth-order constitutive tensor given by Eq. (83) resulting from the microplane theory does not follow the form given by Eq. (57). To make the formulation compatible with Eq. (57), instead of using Eq. (83), one can use Eq. (57) directly with the damage variables defined as the mean stiffness degradation of all the microplanes, namely,

$$\omega_t = 1 - \frac{3}{2\pi}\oint_S \frac{\mathcal{E}_N}{\mathcal{E}_{N0}}\mathrm{d}S; \omega_s = 1 - \frac{3}{2\pi}\oint_S \frac{\mathcal{E}_T}{\mathcal{E}_{T0}}\mathrm{d}S. \tag{84}$$

Remark 2. We note that while higher-order microplane models were formulated before (see, e.g., Lale et al., 2017; Ožbolt and Gambarelli, 2018; Lale and Cusatis, 2021), these approaches included only the strain gradient and missed the important effect of material rotation gradient, which is included in the sprain tensor.

5. Discretization using isogeometric analysis

The discrete equations of mechanical equilibrium (under the small-strain assumption) are obtained using a standard Galerkin technique (Belytschko et al., 2014; Hughes, 2012). We assume that the ith Cartesian component of the displacement field is approximated as

$$u_i^h = \sum_A \boldsymbol{N}^A u_i^A, \tag{85}$$

where A is the nodal index, $\boldsymbol{N}^A$ is the basis function associated with node A, and u_i^A is the nodal displacement unknown. Introducing the displacement approximation in the weak form of the governing equations of mechanical equilibrium results in the following semi-discrete equations:

$$\int_V \left(\sigma_I \boldsymbol{B}_{Ii}^A + \tau_{Ik}\boldsymbol{P}_{Iik}^A\right)\mathrm{d}V = \int_S \boldsymbol{N}^A t_i^{\mathrm{ext}} dS + \int_V \boldsymbol{N}^A b_i \mathrm{d}V - \int_V \boldsymbol{N}^A \rho \ddot{u}_i \mathrm{d}V. \tag{86}$$

Here, $I = 1, \dots, 3$ in 2D and $I = 1, \dots, 6$ in 3D, is the index of the Voigt notation, t_i^{ext}, b_i and ρ are the external traction, body force per unit volume and the solid mass density, respectively, $\boldsymbol{B}_{Ii}^A$ is the standard strain–displacement matrix given by

$$\boldsymbol{B}_{Ii}^A = \begin{bmatrix} \boldsymbol{N}_{,x_1}^A & 0 \\ 0 & \boldsymbol{N}_{,x_2}^A \\ \boldsymbol{N}_{,x_2}^A & \boldsymbol{N}_{,x_1}^A \end{bmatrix} \tag{87}$$

in 2D and by

$$\boldsymbol{B}_{Ii}^A = \begin{bmatrix} \boldsymbol{N}_{,x_1}^A & 0 & 0 \\ 0 & \boldsymbol{N}_{,x_2}^A & 0 \\ 0 & 0 & \boldsymbol{N}_{,x_3}^A \\ 0 & \boldsymbol{N}_{,x_3}^A & \boldsymbol{N}_{,x_2}^A \\ \boldsymbol{N}_{,x_3}^A & 0 & \boldsymbol{N}_{,x_1}^A \\ \boldsymbol{N}_{,x_2}^A & \boldsymbol{N}_{,x_1}^A & 0 \end{bmatrix} \tag{88}$$

in 3D. In addition, in Eq. (86), a new quantity $\boldsymbol{P}_{Iik}^A$ emerges, which we call the *sprain-displacement matrix* given by

$$\boldsymbol{P}_{Ii1}^A = \begin{bmatrix} \boldsymbol{N}_{,x_1x_1}^A & 0 \\ 0 & \boldsymbol{N}_{,x_2x_1}^A \\ \boldsymbol{N}_{,x_2x_1}^A & \boldsymbol{N}_{,x_1x_1}^A \end{bmatrix}; \boldsymbol{P}_{Ii2}^A = \begin{bmatrix} \boldsymbol{N}_{,x_1x_2}^A & 0 \\ 0 & \boldsymbol{N}_{,x_2x_2}^A \\ \boldsymbol{N}_{,x_2x_2}^A & \boldsymbol{N}_{,x_1x_2}^A \end{bmatrix} \tag{89}$$

in 2D and by

$$\boldsymbol{P}_{Ii1}^A = \begin{bmatrix} \boldsymbol{N}_{,x_1x_1}^A & 0 & 0 \\ 0 & \boldsymbol{N}_{,x_2x_1}^A & 0 \\ 0 & 0 & \boldsymbol{N}_{,x_3x_1}^A \\ 0 & \boldsymbol{N}_{,x_3x_1}^A & \boldsymbol{N}_{,x_2x_1}^A \\ \boldsymbol{N}_{,x_3x_1}^A & 0 & \boldsymbol{N}_{,x_1x_1}^A \\ \boldsymbol{N}_{,x_2x_1}^A & \boldsymbol{N}_{,x_1x_1}^A & 0 \end{bmatrix}; \boldsymbol{P}_{Ii2}^A = \begin{bmatrix} \boldsymbol{N}_{,x_1x_2}^A & 0 & 0 \\ 0 & \boldsymbol{N}_{,x_2x_2}^A & 0 \\ 0 & 0 & \boldsymbol{N}_{,x_3x_2}^A \\ 0 & \boldsymbol{N}_{,x_3x_2}^A & \boldsymbol{N}_{,x_2x_2}^A \\ \boldsymbol{N}_{,x_3x_2}^A & 0 & \boldsymbol{N}_{,x_1x_2}^A \\ \boldsymbol{N}_{,x_2x_2}^A & \boldsymbol{N}_{,x_1x_2}^A & 0 \end{bmatrix}$$

$$\boldsymbol{P}_{Ii3}^A = \begin{bmatrix} \boldsymbol{N}_{,x_1x_3}^A & 0 & 0 \\ 0 & \boldsymbol{N}_{,x_2x_3}^A & 0 \\ 0 & 0 & \boldsymbol{N}_{,x_3x_3}^A \\ 0 & \boldsymbol{N}_{,x_3x_3}^A & \boldsymbol{N}_{,x_2x_3}^A \\ \boldsymbol{N}_{,x_3x_3}^A & 0 & \boldsymbol{N}_{,x_1x_3}^A \\ \boldsymbol{N}_{,x_2x_3}^A & \boldsymbol{N}_{,x_1x_3}^A & 0 \end{bmatrix} \tag{90}$$

in 3D. Linearization of the internal work terms in the Galerkin formulation given by Eq. (86) results in the following expression for the left-hand-side stiffness matrix:

$$\begin{aligned} \left(K_{\text{alg}}\right)_{ij}^{AB} = \int_V \Big\{ & \boldsymbol{B}_{Ii}^{A\intercal} \left(\mathbb{C}_{SE}^{\tan}\right)_{IJ} \boldsymbol{B}_{Jj}^B + \boldsymbol{B}_{Ii}^{A\intercal} \left(\mathbb{C}_{S\Xi}^{\tan}\right)_{IJk} \boldsymbol{P}_{Jjk}^B + \\ & \boldsymbol{P}_{Iik}^{A\intercal} \left(\mathbb{C}_{TE}^{\tan}\right)_{IkJ} \boldsymbol{B}_{Jj}^B + \boldsymbol{P}_{Iik}^{A\intercal} \left(\mathbb{C}_{T\Xi}^{\tan}\right)_{IkJm} \boldsymbol{P}_{Jjm}^B \Big\} \, \mathrm{d}V, \end{aligned} \tag{91}$$

where the tangent stiffness tensors $\mathbb{C}^{\tan}$ are given by

$$\left(\mathbb{C}_{SE}^{\tan}\right)_{IJ} = \frac{\partial \sigma_I}{\partial \varepsilon_J}; \left(\mathbb{C}_{S\Xi}^{\tan}\right)_{IJk} = \frac{\partial \sigma_I}{\partial \xi_{Jk}}; \left(\mathbb{C}_{TE}^{\tan}\right)_{IkJ} = \frac{\partial \tau_{Ik}}{\partial \varepsilon_J}; \left(\mathbb{C}_{T\Xi}^{\tan}\right)_{IkJm} = \frac{\partial \tau_{Ik}}{\partial \xi_{Jm}}. \tag{92}$$

Calculation of the sprain terms in Eq. (86) makes use of the second derivatives of the displacement field and the corresponding test functions. As a result, the proposed approach must rely on the approximation that is at least C^1-continuous. While several options are available, we choose to discretize the equations using IGA based on Non-Uniform Rational B-Splines (NURBS) (Hughes et al., 2005). The geometric modeling flexibility combined with higher-order accuracy and smoothness of IGA has led to its superior performance for a variety of solid and structural mechanics systems (Hughes et al., 2005; Cottrell et al., 2009; Pigazzini et al., 2018; Alaydin et al., 2021; Li et al., 2022; Li and Bazilevs, 2023) and it is felt that IGA is particularly well suited for the present application.

6. Computational results

Unless otherwise stated, all the present examples use quadratic NURBS with C^1-continuity.

6.1. 1D bar in tension

We consider a 1D bar of length L under tension as illustrated in Fig. 2a. The governing equations are the 1D counterparts of Eqs. (22)–(24) with the boundary conditions

$$u(0) = 0; u(L) = \bar{u} > 0. \tag{93}$$

A material point at the mid-span is assumed to be slightly weaker than ones in the rest of the bar. This set-up triggers damage at this point, ensuring a deterministic and unique result. We use a constitutive law described by Eqs. (29)–(33) (see Fig. 2b), in which the equivalent strain $\bar{\chi}$ is computed from $\epsilon = \mathrm{d}u/\mathrm{d}x$ and $\xi = \mathrm{d}^2u/\mathrm{d}x^2$. The initial fracture energy of the material is of the form $G_f = 0.5 g_f w_{\text{char}}$, where w_{char} is a length scale representing the size of inhomogeneity in the quasibrittle material and g_f is defined as in Eq. (34).

The computational results are shown in Fig. 3 using a mesh size of $h = L/20$. Both linear (for $l_t = 0$) and quadratic (for $l_t > 0$) NURBS of maximal continuity are considered. Note that linear NURBS are equivalent to linear finite elements. Figs. 3a, d show that the localization of the strain appears at the pre-damaged location.

When l_t is non-zero, the localizing strain spreads over a few knot spans. The spreading extends further when l_t is increased (see Figs. 3e, f). The stress profile is no longer constant due to the presence of the spress τ. This regularization effect is explained by the emergence of the sprain ξ (see Figs. 4a–c), which is symmetric about the pre-damaged region, and the corresponding spress, which suppresses abrupt changes in the strain field. The distribution of sprain exhibits convergence under mesh refinement.

Remark 3. Similarly to l_t, w_t also has a spreading effect on the localized strain. However, it is only effective when used with non-zero l_t. A more detailed discussion can be found in Appendix E.

The force–displacement curves (Fig. 4d) support the fact that strain regularization corrects the pathological mesh-dependence behavior of the discrete solution. When $l_t = 0$, for linear finite elements, the strain will always localize in one element whose size can be reduced, theoretically, to zero. This causes the unrealistic deviation between the solid and dashed curves (corresponding to the $h = L/20$ and $h = L/40$ computations, respectively) of the force–displacement response shown in Fig. 4d. However, when l_t is non-zero, this deviation vanishes and the results converge under mesh refinement.

Remark 4. Energy dissipated by the damaged bar can be computed from g_f (see Eq. (34)) and characteristic length w_{char}. The latter may be estimated as

$$w_{\text{char}} = 1.32 \left[1 + w_1 \left(\frac{E}{E_t} \right)^{w_2} \right] (l_t + l_{t0}). \tag{94}$$

Here $w_1 = 2.27;\ w_2 = 0.356$, and l_{t0} is an intrinsic localization limiter of a numerical method (e.g., local mesh size). The softening slope, in the case of continuum damage model, is given by $E_t = f_t/(e_f - e_0)$. The derivation of w_{char} is summarized in Appendix F.

6.2. Comparison of the nodal sprain forces

In the original development of the sCBM (Zhang and Bažant, 2023), a different approach was used. On a regular Cartesian mesh, the curvature of the displacement vector (or the second derivatives of the hessian of the vectorial displacement field) was represented by its finite difference approximation. Then the derivatives of the sprain energy with respect to the nodal displacements provided self-equilibrated forces, called the sprain forces, that had to be applied to resist excessive curvature (the sprain forces represented the spress multiplied by the tributary volume of each node) Note that the use of finite differences required construction of a Cartesian mesh around the notch tip. In the 1D setting, two schemes were used to distribute the forces to the nodes: (a) The "triplet" case in 1D, in which the computed nodal sprain force $\bar{f}$ was distributed to the node and its nearest left and right neighbors as $f_{\text{sCBM}} = [-\bar{f}, 2\bar{f}, -\bar{f}]^T$; (b) The "quintuplet" case in which the computed nodal sprain force $\bar{f}$ was distributed to the node and its four nearest as $f_{\text{sCBM}} = [-\bar{f}, -\bar{f}, 4\bar{f}, -\bar{f}, -\bar{f}]^T$.

In the IGA-based isCBM formulation, the nodal sprain forces come from the sprain terms in the semi-discrete weak formulation given by Eq. (86) and are consistent with the choice of NURBS approximation:

$$f_{\text{isCBM}} = \int_V \tau_{Ik} \boldsymbol{P}^A_{Iik} \mathrm{d}V. \tag{95}$$

Fig. 5 shows a comparison between f_{isCBM} and f_{sCBM} for the 1D bar problem. Note that the sprain force $\bar{f}$ is scaled such that its magnitude is comparable to the maximum of f_{isCBM}. Fig. 5 shows that the two nodal force definitions show a very similar profile, with the degree of similarity increasing with the increasing order and smoothness of the NURBS approximation. In addition, both nodal force fields vanish at the boundary as desired. These results suggest that the form of the sprain forces designed at the discrete level in sCBM to achieve the desired strain regularization outcomes is naturally reproduced in the variational framework of isCBM.

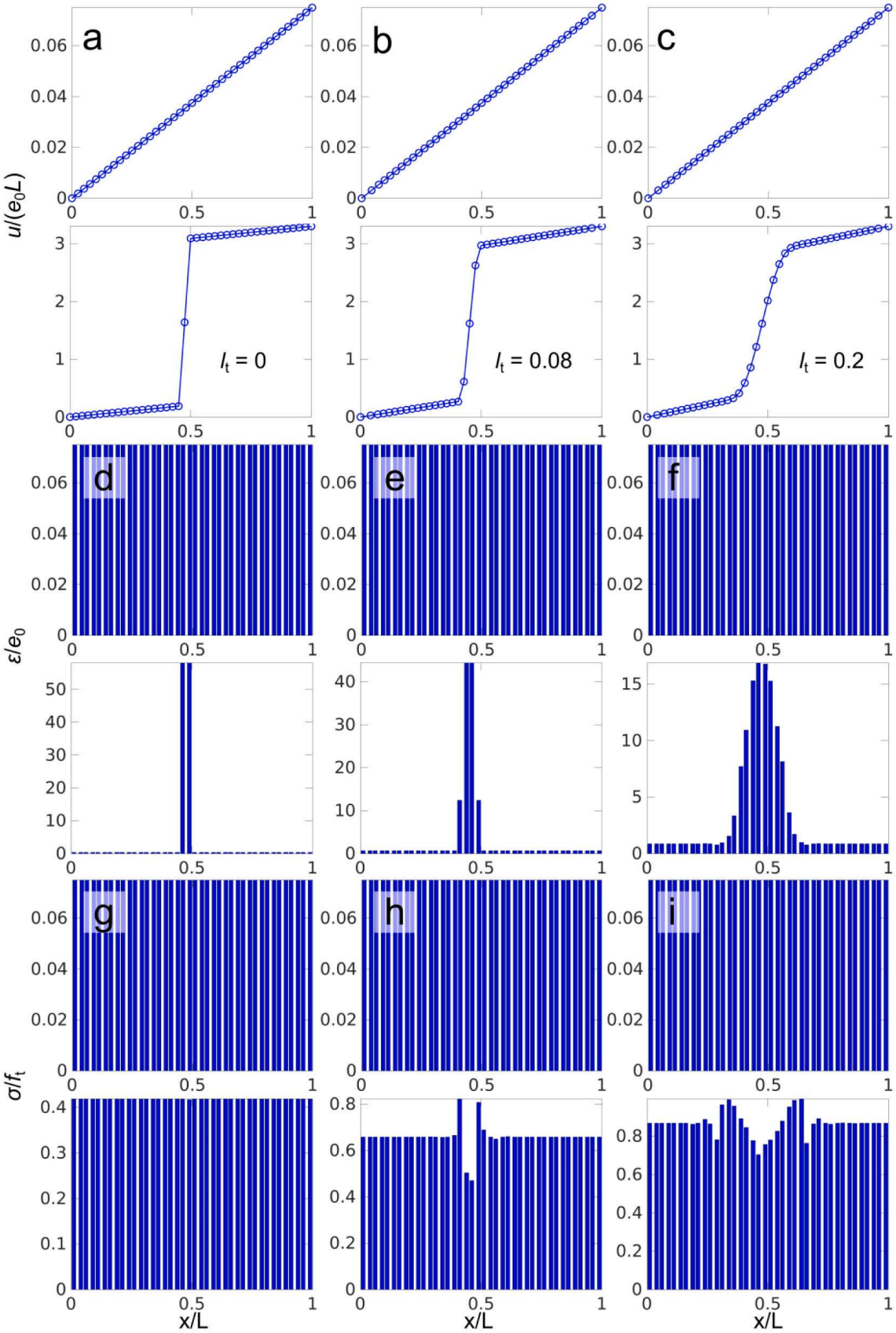

Fig. 3. Normalized displacement, strain and stress fields in the 1D bar for $\bar{u} = 0.07\epsilon_0 L$ and $\bar{u} = 3.2\epsilon_0 L$; (a, d, g) $l_t = 0$; (b, e, h) $l_t = 0.08$ mm; and (c, f, i) $l_t = 0.2$ mm. The knot span $h = L/20$ and $L = 10$ mm.

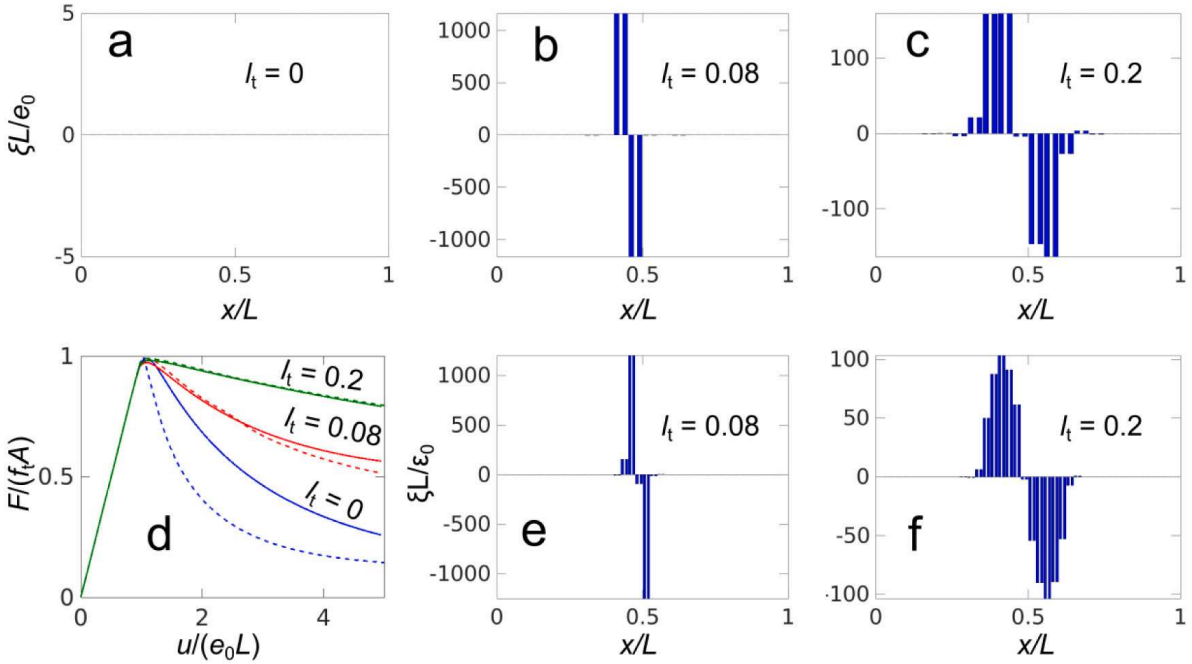

Fig. 4. (a)–(c) Normalized ξ-field (defined by Eq. (13)) in the 1D bar when $l_t = 0; 0.08; 0.2$ mm (knot span $h = L/20$ and $L = 10$ mm); (d) Normalized force–displacement curves (A is the cross-section area of the bar); and (e), (f) Consistency of the normalized ξ-field when the mesh is refined (knot span $h = L/40$).

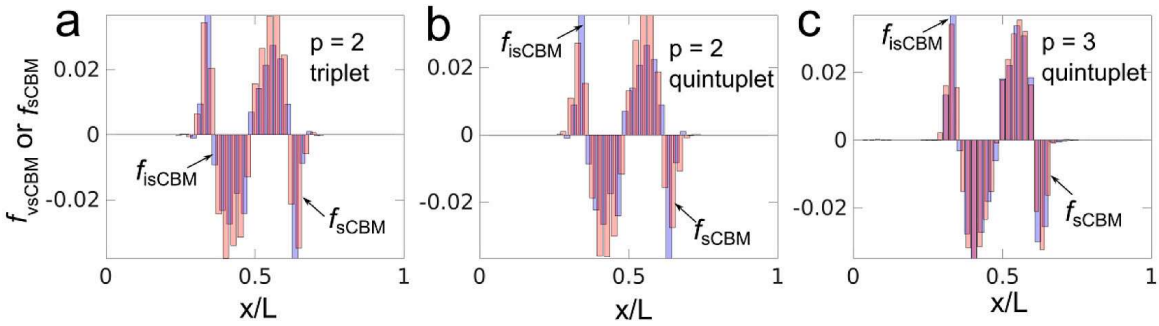

Fig. 5. Comparison of the nodal sprain forces for the 1D bar problem. To enhance the clarity of the figure, the locations of the bars in the bar graph are intentionally selected such that f_{isCBM} and f_{sCBM} are visually distinctive.

6.3. *Three-point bending of notched beams: Alleviating mesh-direction bias*

We consider a single-edge-notch beam subjected to three-point bending. The problem setup is shown in Fig. 6a where we set $D = 50$ mm and $L = 175$ mm. The computations are done using the M7-microplane model (Caner and Bažant, 2013a,b; Nguyen et al., 2021a; Bažant and Oh, 1985; Bažant and Prat, 1988), whose parameters are summarized in Table 1; see Appendix C. Here we make use of the sprain formulation given by Eqs. (55) and (84), and refer to it as the *partial* approach. The *total* approach makes use of the sprain formulation given by Eq. (83). A comparison between the two approaches is provided in the following section.

After the coarsest NURBS mesh is constructed, the control points at the top surface of the beam are displaced in the horizontal direction, which introduces a mesh-direction bias without changing the problem geometry. The mesh is then refined to carry out the computations. The mesh-direction bias is characterized using the angle θ as shown in Fig. 6b. The angle ranges from no deviation ($\theta = 0°$) to an extreme case of $\theta = 40°$. The resulting meshes are shown in Fig. 6c.

For this setup, independent of how skewed the mesh is, the cracks should propagate straight up. However, the local nature of damage is well known to produce mesh-dependent solutions. In this case, the damage zone clearly follows the mesh direction as shown in Fig. 6d. This, in turn, generates significant differences in the force–displacement curves at the structure level for both the peak load and softening slope, as shown in Fig. 6h. The case of non-zero l_t is able to alleviate the mesh direction bias as shown in Fig. 6e. Fractures no longer localize in a narrow band of elements and propagate mainly in the vertical direction. This mesh-independent nature of the solution yields consistent force–displacement results for both the peak load and softening slope (see Fig. 6e).

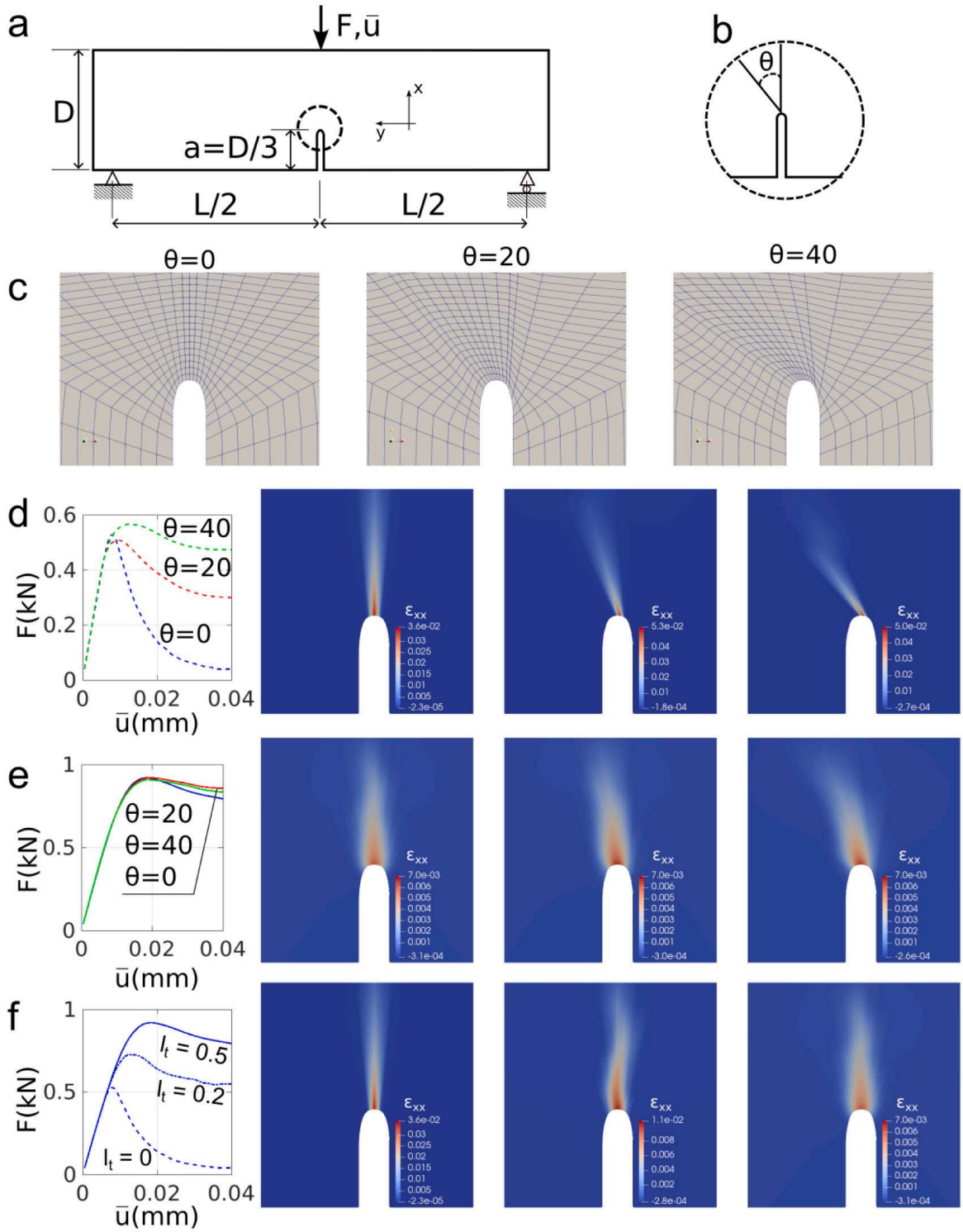

Fig. 6. Notched beam subjected to three-point bending. (a) Problem setup; (b) Definition of the mesh bias angle θ; (c) Problem meshes for different values of θ; (d)–(e) Directional bias in the solution, which is corrected by the isCBM when l_t increases from 0.0 mm (d) to 0.5 mm (e); (f) The effect of l_t on the fracture energy, apparent structure strength and post-peak behavior.

Figs. 6d–f show that both the mesh-size and direction objectivity of the results improves as l_t increases. The FPZ also grows in size and changes shape leading to a higher peak load in the force–displacement curve in Fig. 6f. Parameter l_t controlling the FPZ size should, therefore, be carefully considered and included in the model calibration process.

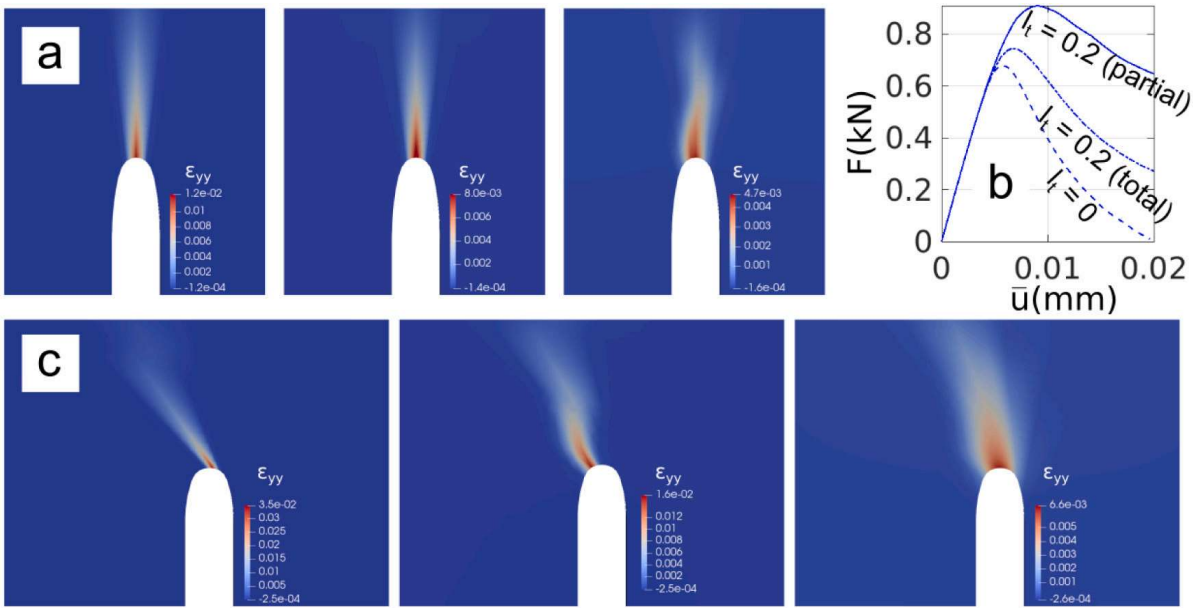

Fig. 7. (a)–(b) Effectiveness of the partial vs total formulation in distributing the strain over the FPZ for the l_t(= 0.2 mm) with $\theta = 0$; (c) Effectiveness of the partial vs total formulation in correcting the mesh-direction bias.

6.4. Comparison between the total and partial sprain formulation of the M7 model

In this section, we compare the performance of the partial (i.e., using Eqs. (55) and (84)) and total (i.e., using Eq. (83)) isCBM formulations of the M7 model. Fig. 7a shows that the partial approach has a stronger regularizing effect on the FPZ as opposed to the total case, which gives a more localized distribution of ϵ. This trend can also be observed in the force–displacement curves in Fig. 7b, which shows a lower failure load and a more brittle post-peak response (i.e., steeper softening) for the total case. Finally, as evidenced in Fig. 7c, the partial approach is also more effective than the total in alleviating the mesh-direction bias. However, despite the somewhat underwhelming performance demonstrated, we believe the total approach may be improved further to achieve better performance, which we leave to the future work. For the remainder of the section we will employ the partial approach, which appears to be robust, and relatively simple to implement.

6.5. Experimental validation

6.5.1. Size effect test

The size effect test is an efficient and distinctive way (Bažant and Nguyen, 2023) to determine the FPZ size and initial fracture energy of the material. Based on a common experimental setup, e.g., the three-point-bending test configuration of single-edge-notched beams (Figs. 8a–b), the tests are performed on scaled specimens (Bažant and Kazemi, 1990; Bažant and Planas, 1998). After obtaining a peak load for each case, a fitting procedure is used to obtain both the initial fracture energy G_f and the characteristic size of the FPZ c_f (Nguyen et al., 2020a,b, 2021b; Dönmez et al., 2023) via the following equations:

$$\sigma_N = \frac{\sigma_0}{\sqrt{1 + D/D_0}}; G_f = \sigma_0^2 D_0 g_0 / E, \; c_f = g_0 D / g_0' \tag{96}$$

where g_0 and g_0' are the dimensionless function that describes the geometry of the beams and its derivative.

Here, experiments by Grégoire et al. (2013) are chosen to validate the proposed framework. Fig. 8c shows a consistent increase of the peak load across the specimen sizes when l_t increases from 0 to 0.2 mm. The nominal strengths computed from these peak loads ($\sigma_N = F/bD$, where b is the out-of-plane thickness of the beams) are compared with the experimental results in Fig. 8d, showing a good fit. Notably, in the range of D's considered in the experiments and for $l_t = 0$, the nominal strength approaches a straight line with slope $-1/2$ on a log–log scale at a faster rate. This is because localized cracks generate a relatively small FPZ compared with the structure size. When regularization is applied, quasi-brittle behavior of the material is better represented and the peak force response is much closer to the experimental data.

The good agreement of the isCBM formulation with the size effect tests is not a random coincidence. Indeed, when overlaying the damage zones of the different-size specimens (such a zone is defined by the boundary delimited by the inelastic strain in the y-direction), their sizes and shapes are almost identical. It is worth noting the non-vanishing width of the FPZ, which becomes important when crack-parallel stress is present in the structure (Nguyen et al., 2020a,b).

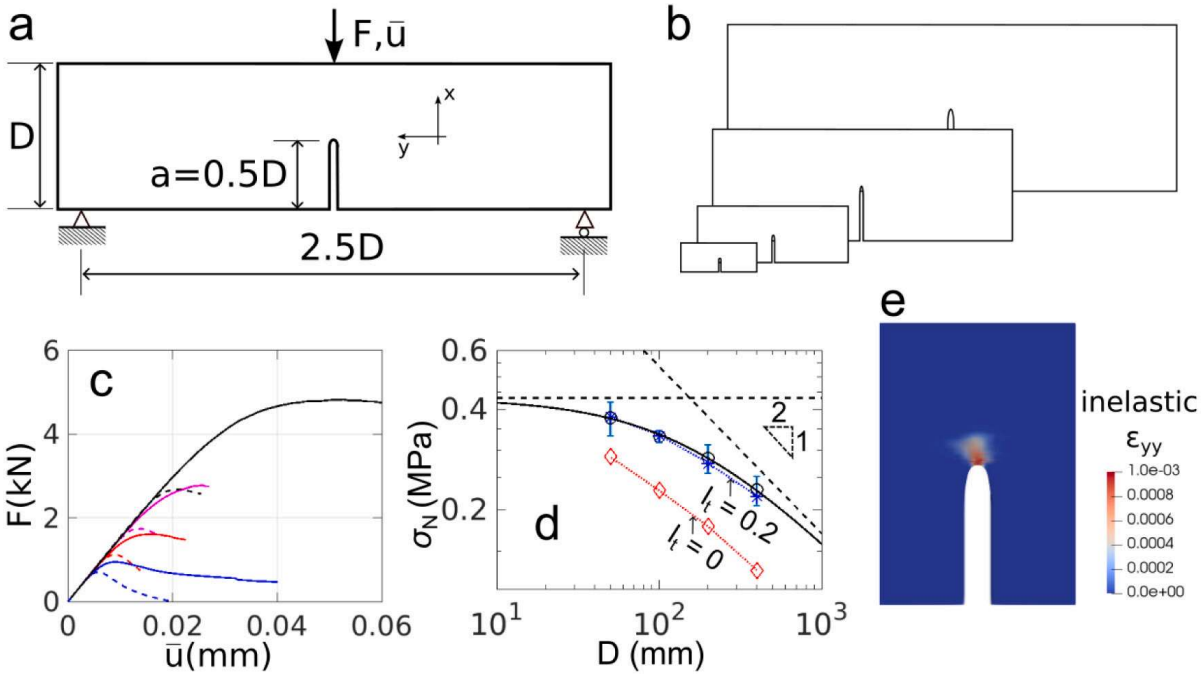

Fig. 8. (a)–(b) Size effect test in which the beams have dimensions $D = 400, 200, 100, 50$ mm; (c) Force–displacement curves for beams of different sizes. Dashed curves represent $l_t = 0$ mm, while solid curves represent $l_t = 0.2$ mm; (d) The predicted nominal strengths are compared with the experimental data, showing good agreement of the sprain formulation with the size effect law; capturing this effect is possible due to the existence of a finite-size FPZ ahead of the tip whose size remains relatively consistent among the beams of different sizes (e).

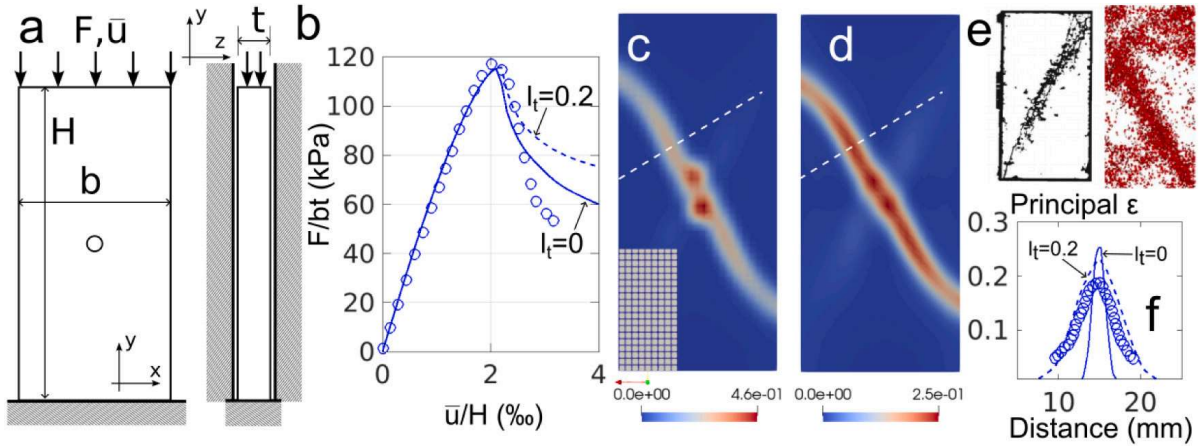

Fig. 9. (a) Sandstone prism subjected to biaxial compression under plane-strain conditions. Here, $H = 100$ mm, $b = 50$ mm, and $t = 50$ mm; (b) Force–displacement curves for $l_s = 0$ mm and $l_s = 0.2$ mm compared with the experimental data. Shear band profile for $l_s = 0$ mm (c) and $l_s = 0.2$ mm (d). Microcrack patterns of cemented rocks (Geel, van, 1995; Wen et al., 2023) (e) and strain profile measured by the digital image correlation (DIC) technique (Wang et al., 2019) (f), confirming the enhanced shear band width that is well captured by the isCBM.

Remark 5. In some cases, the aggregate may be chemically weakened leading to through-aggregate cracks with near-zero width (Zhou et al., 2021). For this, Eq. (55) may be modified to adapt to such cases where β can be made a function of a chosen chemical potential reducing the crack band width to account for this weakening effect.

6.5.2. Regularization of a shear band

The current framework is not limited to opening-mode cracks and naturally applies to other phenomena such as localized shear or diagonal splitting bands. To demonstrate this, we carry out simulations of an experiment on sandstone under plane-strain biaxial compression (Wen et al., 2023). At the front and back surfaces of the specimen, a rigid frame was attached to constrain the z-displacement. At the side surfaces, in the x-direction, pressure was applied to vary the biaxiality of the stress state (here we consider only the case pf zero confining pressure). A compressive displacement was applied to the top and bottom surfaces of the specimen. See Fig. 9(a) for the problem setup.

In the case of $l_s = 0$ (see Fig. 9c), the shear deformation is localized into a narrow band whose size scales with the local mesh size and is smaller than the inhomogeneity length scale of the material. As a result, the predicted force–displacement curve shows a slightly softer behavior compared with the experimental data (see Fig. 9b). When $l_s = 0.2$ mm, the width of the shear band expands (see Fig. 9d), leading to a better match with the experimental results. Note the difference between the numerical and experimental curves in the post-peak regime. This might be caused by an overestimation of the cohesion-friction transition of the M7 constitutive law for concrete, which needs to be re-calibrated for sandstone.

The difference in the load–displacement curves is not sufficient for reaching a definitive conclusion and thus requires additional validation. For this, a comparison is made between the simulation results and digital image correlation (DIC) measurements for the microcrack patterns and strain profile across the band (Wen et al., 2023; Geel, van, 1995; Wang et al., 2019) in Figs. 9e–f. The maximum principal strain profiles, measured across the shear band and shown in Fig. 9f, revealed that the strain profile is spread within a finite-size band, which is well captured by the isCBM formulation. Finite width shear bands (or diagonal splitting bands) appear to be common among cemented rocks where the microcracks contribute to the dissipation of inelastic energy prior to a major failure (see Fig. 9e).

It is worth noting that in some cases of dynamic shear, the release of energy may be so abrupt that a large amount of released heat suffices to weaken the mechanical properties of aggregate, which may lead to a near-zero-thickness shear band (Rice, 2006) ($l_s \approx 0$). In this case, l_s or β can be made a function of inelastic work and gradually reduced to zero as the state variables reach their critical values.

Remark 6. The present formulation of the sprain microplane model has been driven by simplicity. In future work all the distinctive tests studied in Bažant and Nguyen (2023) should be simulated and it is expected that a refinement of the sprain microplane would be required. Nevertheless present formulation suffice to demonstrate the viability of the isCBM.

7. Conclusions

1. The present IGA formulation of the smooth crack band theory based on the hessian tensor of the displacement field (i.e., the sprain deformation tensor) is shown to regularize the strain field of quasibrittle damage and prevent nonphysical excessive localization.
2. The novel homogenization approach is used to explain the emergence of the tensors of sprain (as a deformation characteristic) and spress (as the work-conjugate of sprain tensor representing the sprain energy derivatives with respect to the sprain tensor components). The spress–sprain relation is part of the constitutive law of the material.
3. The analysis revealed two different regularizing material characteristic lengths, one of which couples the strain and sprain deformations, while the other couples the spress and sprain tensors in the constitutive law and equilibrium equations.
4. These lengths, together with the damage law, ensure the correct fracture energy and damage zone width, length and shape, reflecting the material physics.
5. An attractive feature of the present methodology is that it is, in principle, applicable to any material model. This is attested by the present study of the isCBM formulation using a simple bar-in-tension problem, combined with the M7 microplane model of concrete failure. This is documented by computer simulations of the size effect and shear band localization.
6. The isogeometric analysis (IGA) provides a natural and convenient way to achieve the complete C^1-continuity of the discretization required to implement the isCBM formulation. It clearly demonstrates that the resulting IGA-based sCBM framework, accompanied by the M7 model of concrete failure, is able to remove the spurious mesh-size dependence of the discrete solutions and is also effective in correcting the mesh-orientation bias of regular meshes.
7. The size and shape of the fracture process zone and the fracture energy are here shown to match the size-effect experiments. The size effect is one of the distinctive tests to validate emerging computational methods for fracture.
8. Moreover, the present formulation is able to regularize the shear-band width in quasibrittle materials, with a regularizing length chosen as independent of the opening-mode damage. This attests to the versatility and general-purpose applicability of the present method.

CRediT authorship contribution statement

Hoang Nguyen: Conceptualized and designed the research, Formulated the mathematical description, Wrote computational codes, Performed the numerical simulations, Analyzed the results, Writing – original draft. **Weican Li:** Performed the numerical simulations, Analyzed the results, Writing – original draft. **Zdeněk P. Bažant:** Conceptualized and designed the research, Analyzed the results, Writing – original draft. **Yuri Bazilevs:** Conceptualized and designed the research, Analyzed the results, Writing – original draft.

Declaration of competing interest

The authors declare that they have no known competing financial interests or personal relationships that could have appeared to influence the work reported in this paper.

Data availability

No data was used for the research described in the article.

Acknowledgments

This work was supported through the Office of Naval Research (ONR) Grant No. N00014-21-1-2670 to Brown University. Additional partial support was also obtained under National Science Foundation (NSF) Grant CMMI-2029641 to Northwestern University.

Appendix A. Derivation of P, Q from S, T, Ξ, E, F, and η

Because the incremental work must be preserved regardless of the sprain deformation tensor, the following equation must hold:

$$S_{IJ}\delta E_{IJ} + T_{IJK}\delta \Xi_{IJK} = \left(F_{QJ}S_{JI} + T_{IJK}\eta_{JKQ}\right)\delta F_{QI} + F_{QI}T_{IJK}\delta\eta_{JKQ} \tag{97}$$

From the definition of η_{IJK}, it is obvious that it has the same symmetry of Ξ_{IJK}. Taking the time derivative of Eq. (8) gives:

$$\delta E_{IJ} = 0.5\left(\delta F_{RI}F_{RJ} + F_{RI}\delta F_{RJ}\right), \tag{98}$$

$$\delta \Xi_{IJK} = 0.5\left(\delta\eta_{JKQ}F_{QI} + \eta_{JKQ}\delta F_{QI} + \delta\eta_{IKQ}F_{QJ} + \eta_{IKQ}\delta F_{QJ}\right) \tag{99}$$

Therefore,

$$\begin{aligned} &S_{IJ}\delta E_{IJ} + T_{IJK}\delta \Xi_{IJK} = 0.5\left(S_{IJ}\delta F_{RI}F_{RJ} + S_{IJ}F_{RI}\delta F_{RJ}\right) + \\ &0.5\left(T_{IJK}\delta\eta_{JKQ}F_{QI} + T_{IJK}\eta_{JKQ}\delta F_{QI} + T_{IJK}\delta\eta_{IKQ}F_{QJ} + T_{IJK}\eta_{IKQ}\delta F_{QJ}\right) \end{aligned} \tag{100}$$

Due to the symmetry, we can rewrite:

$$S_{IJ}\delta E_{IJ} + T_{IJK}\delta \Xi_{IJK} = \left(F_{QJ}S_{JI} + T_{IJK}\eta_{JKQ}\right)\delta F_{QI} + F_{QI}T_{IJK}\delta\eta_{JKQ} \tag{101}$$

Comparing Eqs. (97) and (101) and altering the indices, we obtain:

$$\boxed{Q_{IJK} = \underset{I,J}{\text{sym}}\left(F_{KQ}T_{QIJ}\right)} \tag{103}$$

and

$$\boxed{P_{IJ} = F_{IQ}S_{QJ} + \eta_{QKI}T_{JQK}} \tag{104}$$

It should be noted that P_{IJ} and Q_{IJK} are naturally coupled through the deformation gradient and sprain deformation tensors. Therefore, unlike the conventional definition of the PK1 stress, the mesoscale spress and sprain terms also contribute to P_{IJ}.

Appendix B. A complete decomposition of a sixth-order isotropic tensor

$$\left(\mathbb{T}_1\right)_{IJKPQR} = \delta_{IJ}\delta_{PQ}\delta_{KR} \tag{105}$$

$$\left(\mathbb{T}_2\right)_{IJKPQR} = \frac{1}{2}\left(\delta_{IP}\delta_{JQ} + \delta_{IQ}\delta_{JP}\right)\delta_{KR} \tag{106}$$

$$\left(\mathbb{T}_3\right)_{IJKPQR} = \frac{1}{2}\left(\delta_{IK}\delta_{JR} + \delta_{IR}\delta_{JK}\right)\delta_{PQ} \tag{107}$$

$$\left(\mathbb{T}_4\right)_{IJKPQR} = \frac{1}{2}\left(\delta_{KP}\delta_{QR} + \delta_{PR}\delta_{KQ}\right)\delta_{IJ} \tag{108}$$

$$\left(\mathbb{T}_5\right)_{IJKPQR} = \frac{1}{4}\left[\left(\delta_{IP}\delta_{JR} + \delta_{IR}\delta_{JP}\right)\delta_{KQ} + \left(\delta_{IQ}\delta_{JR} + \delta_{IR}\delta_{JQ}\right)\delta_{KP}\right] \tag{109}$$

$$\left(\mathbb{T}_6\right)_{IJKPQR} = \frac{1}{4}\left[\left(\delta_{IP}\delta_{QR} + \delta_{IQ}\delta_{PR}\right)\delta_{JK} + \left(\delta_{JP}\delta_{QR} + \delta_{JQ}\delta_{PR}\right)\delta_{IK}\right] \tag{110}$$

The linear system with six variables that results in Eq. (56)

$$\frac{2}{5}\tilde{\lambda}_1 - \frac{1}{5}\tilde{\lambda}_2 - \frac{1}{15}\tilde{\mu}_1 - \frac{1}{3}\tilde{\mu}_2 = (1-\omega)\frac{l_t^2}{12}\lambda; \tag{111}$$

$$\frac{1}{3}\tilde{\mu}_1 + \frac{2}{3}\tilde{\mu}_2 = (1-\omega)\frac{l_t^2}{12}2\mu; \tag{112}$$

$$\frac{2}{5}\tilde{\lambda}_3 - \frac{1}{5}\tilde{\lambda}_4 - \frac{2}{15}\tilde{\mu}_1 + \frac{1}{3}\tilde{\mu}_2 = 0; \tag{113}$$

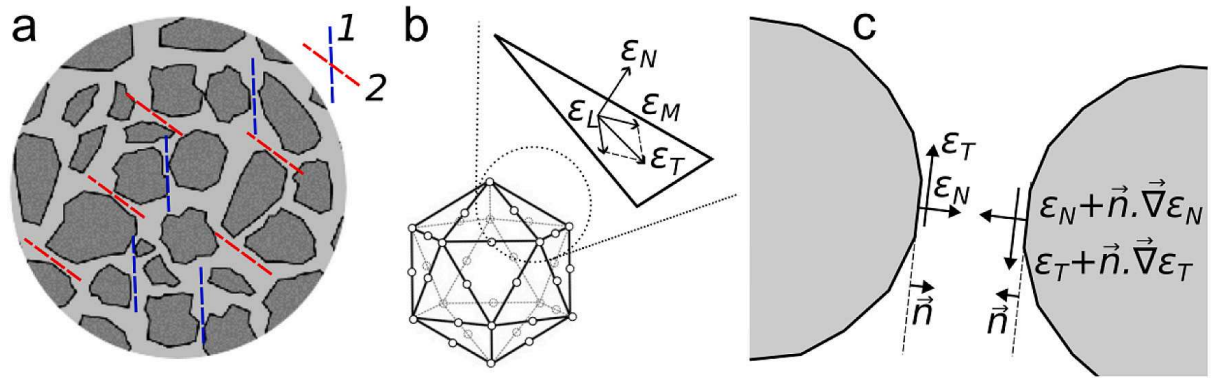

Fig. Appendix-1. (a) In concrete, the constitutive law can be constructed via the mesoscale behaviors of microplanes. For example, interactions between two aggregates across the one plane can be lumped into microplane 1, while those across come other inclined plane are lumped into microplane 2; (b) the microplane strain vectors, including the normal, ε_N, and tangential (shear) components, ε_T, represent the projections of the strain tensor onto each microplane. Through these vectors, the material responses are formulated according to the microplane constitutive law; (c) the variation of the normal and tangential strain vectors in the normal direction.

$$-\frac{1}{5}\tilde{\lambda}_1+\frac{3}{5}\tilde{\lambda}_2-\frac{2}{15}\tilde{\mu}_1+\frac{1}{3}\tilde{\mu}_2=0; \tag{114}$$

$$\frac{2}{3}\tilde{\mu}_1-\frac{2}{3}\tilde{\mu}_2=0; \tag{115}$$

$$-\frac{1}{5}\tilde{\lambda}_3+\frac{3}{5}\tilde{\lambda}_4-\frac{4}{15}\tilde{\mu}_1-\frac{1}{3}\tilde{\mu}_2=0 \tag{116}$$

Appendix C. A summary of microplane model

While the tensorial models construct the relation between the stress and strain tensors using tensorial invariants together with loading surfaces, normality rules, plastic-hardening parameter(s) and damage parameter(s), the microplane constitutive model does the same with a vectorial formula (Bažant and Planas, 1998; Bažant et al., 2021; Bažant and Oh, 1985). In this type of constitutive law, the strain vectors are computed based on the projection of the strain tensor onto generic planes of arbitrary normal directions, called the microplanes. The use of vectors instead of tensors assists the physical insight, intuitively reflecting the microcrack openings, splitting, shear slip and frictional dilatancy (see Fig. Appendix-1 for a clear illustration). The microplane theory has been applied to concrete (both plain and fiber-reinforced), fiber composites, shale and other anisotropic rocks, soils, metals, elasto-plastic metals (Brocca and Bažant, 2000), shape-memory alloys, and ceramics subjected to monotonic, cyclic, and sustained loadings. The microplane model has also been generalized to fatigue up to several thousand load cycles (Kirane and Bažant, 2015).

M7 (Caner and Bažant, 2013a,b) is the latest in a series of progressively improved concrete models starting in 1985 with M1. In this model, all of the inelastic behaviors are characterized by stress–strain boundaries, and the return to a boundary is done at a constant strain in each loading step (this is a special case of the radial return algorithm). The energy dissipation on the microplane level is guaranteed to be non-negative. Hence the non-associated plasticity with its computational limitations is made unnecessary and apparent violation the normality rule in the stress space does not matter since the impossibility of negative dissipation is guaranteed vectorially on the microplanes. There is no possibility of negative dissipation due to unequal friction and dilatancy angles. Through a properly weighted integration over all spatial orientations (Bažant and Oh, 1986; Stroud, 1971), the stress tensor is obtained by the variational principle of virtual work. A numerical integration over a hemispherical surface is carried out according to an optimal Gaussian formula whole integration points, with certain weights, represent the discrete orientations of the microplanes. Although the minimum number of microplanes is 21, typically 37 microplanes are used for better accuracy (Bažant and Oh, 1986)).

On the boundary describing the stress–strain vectorial relations, while a negative slope in the stress–strain plane defines the evolution of damage, a horizontal slope defines plastic yielding. Similar to crystal plasticity models, the interaction of microplanes may generate hardening plasticity or damage at the tensorial level. Moreover, separate damage variables (like ω in the case of continuum damage model in Eq. (29)) is not needed, and the inelastic deformation can be defined by subtracting the elastic deformation from the total one.

As a result of the strain tensor projection, one normal components and one shear component, i.e., ε_N and ε_T (see Fig. Appendix-1), arise on each microplane, the latter of which is then further projected onto two predefined bases tangential to the microplane as ε_L and ε_M. When 37 microplanes per hemisphere (Bažant and Oh, 1986) are used, one has $37\times3=111$ variables driving damage and plasticity, which is equivalent to 111 simultaneous loading surfaces. The strain tensor projection represents a kinematic constraint of the microplanes, which is the opposite of the static constraint in which the stress tensor is projected on the microplanes (the dual static constraint was used in the classical slip theory of plasticity of Batdorf and Budiansky (1949) but in the case of softening damage was found prone to instability).

The multi-surface feature explains why the vertex effect (for the definition and discussions on this effect, see Gerard and Becker (1957), Budiansky (1959), Caner et al. (2002) and Jirásek and Bažant (2001)) can occur at any point of the nine-dimensional

Table 1
M7-microplane model parameters for Sections 6.3–6.5.

Parameters	Sections 6.3–6.4	Section 6.5.1	Section 6.5.2
E	30000	31500	30000
ν	0.18	0.18	0.18
k_1	0.00012	0.00008	0.00003
k_2	80	55	40
k_3	20	15	15
k_4	45	40	40

space of stress tensor, which would not be allowed by the loading surfaces of hardening plasticity. It also is worth noting that the damage generation on softening stress–strain boundaries typically occurs only at some microplanes but not at others, and that loading, unloading or reloading may selectively occur of various microplanes. All this gives rise to a strong and highly varied path-dependence of the microplane constitutive model.

Also note that the generation of damage on a microplane does not proceed monotonically, and that a damaged microplane can regain the stiffness under compression when it is subjected to, for example, hydrostatic pressure. The microplane model allows simplifying the vectorial constitutive law as one-to-one relations between the conjugate stress and strain components on the microplanes. No cross-interactions such as the Poisson effect on the microplanes need to be considered since such cross effects are automatically generated by interaction of microplanes of different orientations.

When the projection is applied to the total strain tensor, the elastic Poisson ratio of the microplane material model cannot exceed 0.25 (Bažant and Oh, 1985). However, Bažant and Prat (1988), Carol and Bazant (1997), Carol et al. (1991) and Bažant et al. (2000) showed that the problem could be solved by decomposition of the normal strain into deviatoric and volumetric components, and projecting each component on the microplanes separately.

It was thought that the microplane model is computationally more demanding than the tensorial constitutive models with invariant. For a finite element (FE) system with about 50 unknowns computer run time is indeed far greater. But the experience with wavecodes such as EPIC (Johnson et al., 1996) or PRONTO (Taylor and Flanagan, 1989) showed that for a system 10 million unknowns the difference is imperceptible. The reason is that the computational work increases linearly with the running time of material model but quadratically with the number of kinematic degrees of freedom.

Several further observations can be made on the incorporation of M7 model into the isCBM framework:

- Both width and length of the FPZ (w_{FPZ} and l_{FPZ}) depend on the constitutive law and the regularizing material characteristic lengths.
- These two independent material characteristic sizes co-exist, implying the inadequacy of any models that confine the cracks into a zero-width line (or surface). The evolution of each size depends on the stress state and the loading path that leads to such stress state, as illustrated in Nguyen et al. (2020a,b).
- A parameterization procedure should start with assuming an l_t that is related to the inhomogeneity size. Next, calibrate the model parameters to match both the shape and size of the FPZ (which is best described by the size effect test, helped by digital image correlation) and the resulting fracture energy.

Calibrated parameters for Sections 6.3–6.5 are summarized below (See Table 1)

We note that the parameters used in this paper were not taken from either (Nguyen et al., 2021a) or (Caner and Bažant, 2013b). This is because in the conventional crack-band model, the crack tends to localize into one element width. Therefore, the parameters are calibrated so that the energy dissipated in that narrow zone reflects the material fracture energy. In isCBM, the FPZ involves multiple element width enclosed within a smooth FPZ, and the parameters should be modified such that the sum of energy dissipated by these elements will reflect the fracture energy.

Appendix D. The relation between second- and third-order linear elastic stress–strain relation based on microplane theory

Stress—a second-order tensor

$$S_{IJ} = \frac{3}{2\pi}\oint_S \left[(\mathcal{E}_N n_I n_J n_P n_Q) + \frac{\mathcal{E}_T}{4}(n_I\delta_{iJ} + n_J\delta_{iI})(n_P\delta_{iQ} + n_Q\delta_{iP} - 2n_P n_Q n_i)\right] \mathrm{d}\mathcal{S}\, E_{PQ}$$
$$= \left[\left(\frac{\mathcal{E}_N - \mathcal{E}_T}{5}\right)\delta_{IJ}\delta_{PQ} + \left(\frac{2\mathcal{E}_N + 3\mathcal{E}_T}{10}\right)(\delta_{IP}\delta_{JQ} + \delta_{IQ}\delta_{JP})\right] E_{PQ} \tag{117}$$
$$= \left[\lambda\delta_{IJ}\delta_{PQ} + \mu(\delta_{IP}\delta_{JQ} + \delta_{IQ}\delta_{JP})\right] E_{PQ} \tag{118}$$

The last equation leads to the definition of $\mathcal{E}_N, \mathcal{E}_T$ in Eqs. (80)–(81). Note that, the following integrals computed on the unit hemisphere $\mathcal{S}$ have been used:

$$\oint_S n_I n_J \mathrm{d}\mathcal{S} = \frac{2\pi}{3}\delta_{IJ} \tag{119}$$

$$\oint_S n_I n_J n_P n_Q \mathrm{d}S = \frac{2\pi}{15}\left(\delta_{IJ}\delta_{PQ} + \delta_{IP}\delta_{JQ} + \delta_{IQ}\delta_{JP}\right) \tag{120}$$

Spress—a third-order tensor

Rewriting Eqs. (77)–(79) and substituting them in the PVW, i.e., Eq. (83), yields:

$$T_{IJK} = \frac{3}{2\pi}\oint_S \Big[(\mathcal{E}_N n_I n_J n_K n_P n_Q n_R) + \frac{\mathcal{E}_T}{4} n_K n_R (n_I n_P \delta_{JQ} + n_I n_Q \delta_{JP} + n_J n_P \delta_{IQ} + n_J n_Q \delta_{IP} - 4 n_I n_J n_P n_Q)\Big] \mathrm{d}S\, \Xi_{PQR} \tag{121}$$

Hence,

$$T_{IJK} = \frac{3}{2\pi}\left[(\mathcal{E}_N - \mathcal{E}_T)\oint_S n_I n_J n_K n_P n_Q n_R \mathrm{d}S + \frac{\mathcal{E}_T}{4}\oint_S n_K n_R \left(n_I n_P \delta_{JQ} + n_I n_Q \delta_{JP} + n_J n_P \delta_{IQ} + n_J n_Q \delta_{IP}\right) \mathrm{d}S \right] \Xi_{PQR} \tag{122}$$

We can apply the following equation:

$$\begin{aligned}\oint_S n_I n_J n_K n_P n_Q n_R \mathrm{d}S = \frac{2\pi}{315}\Big(&\delta_{IJ}\delta_{KP}\delta_{QR} + \delta_{IJ}\delta_{KQ}\delta_{PR} + \delta_{IJ}\delta_{KR}\delta_{PQ} + \\ &\delta_{IK}\delta_{JP}\delta_{QR} + \delta_{IK}\delta_{JQ}\delta_{PR} + \delta_{IK}\delta_{JR}\delta_{PQ} + \\ &\delta_{IP}\delta_{JK}\delta_{QR} + \delta_{IP}\delta_{JQ}\delta_{KR} + \delta_{IP}\delta_{JR}\delta_{KQ} + \\ &\delta_{IQ}\delta_{JK}\delta_{PR} + \delta_{IQ}\delta_{JP}\delta_{KR} + \delta_{IQ}\delta_{JR}\delta_{KP} + \\ &\delta_{IR}\delta_{JK}\delta_{PQ} + \delta_{IR}\delta_{JP}\delta_{KQ} + \delta_{IR}\delta_{JQ}\delta_{KP}\Big)\end{aligned} \tag{123}$$

The third-order stress then reads:

$$\begin{aligned}T_{IJK} = \Bigg[&\frac{(\mathcal{E}_N - \mathcal{E}_T)}{105}\Big(\delta_{IJ}\delta_{KP}\delta_{QR} + \delta_{IJ}\delta_{KQ}\delta_{PR} + \delta_{IJ}\delta_{KR}\delta_{PQ} + \\ &\delta_{IK}\delta_{JP}\delta_{QR} + \delta_{IK}\delta_{JQ}\delta_{PR} + \delta_{IK}\delta_{JR}\delta_{PQ} + \\ &\delta_{IP}\delta_{JK}\delta_{QR} + \delta_{IP}\delta_{JQ}\delta_{KR} + \delta_{IP}\delta_{JR}\delta_{KQ} + \\ &\delta_{IQ}\delta_{JK}\delta_{PR} + \delta_{IQ}\delta_{JP}\delta_{KR} + \delta_{IQ}\delta_{JR}\delta_{KP} + \\ &\delta_{IR}\delta_{JK}\delta_{PQ} + \delta_{IR}\delta_{JP}\delta_{KQ} + \delta_{IR}\delta_{JQ}\delta_{KP}\Big) \\ &+\frac{\mathcal{E}_T}{20}\Big(\delta_{JQ}\delta_{IK}\delta_{PR} + \delta_{JQ}\delta_{IP}\delta_{KR} + \delta_{JQ}\delta_{IR}\delta_{KP} + \\ &\delta_{JP}\delta_{IK}\delta_{QR} + \delta_{JP}\delta_{IQ}\delta_{KR} + \delta_{JP}\delta_{IR}\delta_{KQ} + \\ &\delta_{IQ}\delta_{JK}\delta_{PR} + \delta_{IQ}\delta_{JP}\delta_{KR} + \delta_{IQ}\delta_{JR}\delta_{KP} + \\ &\delta_{IP}\delta_{JK}\delta_{QR} + \delta_{IP}\delta_{JQ}\delta_{KR} + \delta_{IP}\delta_{JR}\delta_{KQ}\Big)\Bigg] \Xi_{PQR}\end{aligned} \tag{124}$$

Appendix E. Effect of w_t

We now take a closer look at the static equilibrium condition (Eq. (22)). Incorporating the constitutive law (Eqs. (29) and (41), assuming zero body force, $b_I = 0$) yields:

$$\frac{\partial}{\partial x}\left[(1-\omega)^2 E\varepsilon\right] - \frac{l_t^2}{12}\frac{\partial^2}{\partial x^2}\left[(1-\omega)^\beta E\xi\right] = 0 \tag{125}$$

with $\beta < 2$. The damage variable is computed from (31) and the equivalent strain reads:

$$\bar{\chi} = \varepsilon + w_t(|\xi| - C) \tag{126}$$

Therefore, in Eq. (125), both w_t and l_t are present. $C = 10^{-10}$ to suppress the noise from round-off errors. The Macaulay bracket is removed as the entire bar is in tension. Two cases can be considered:

(a) $l_t = 0, w_t > 0$

$l_t = 0$ means that the coupling between sprain and spress is non-existent, so the strain profile must satisfy $(1-\omega)^2 E\varepsilon =$ constant. When $w_t = 0$, the strain will localize into one bar so that the unloading and the softening section of the bar must reach the same stress level. However, when $w_t \neq 0$, such a localization will lead to a high $|\xi|$ value, and the damage will arise at the neighboring points. This will result in a violation of the stress equilibrium condition (see Figs. Appendix-2a–c for the first-iteration profiles of the deformation fields). Therefore, the strain and sprain deformations within w_t will redistribute to satisfy the constraint $1-\omega \propto \varepsilon^{-0.5}$. This can only be achieved by a fixed constitutive law, which is both inconvenient and non-physical. Therefore, with a general

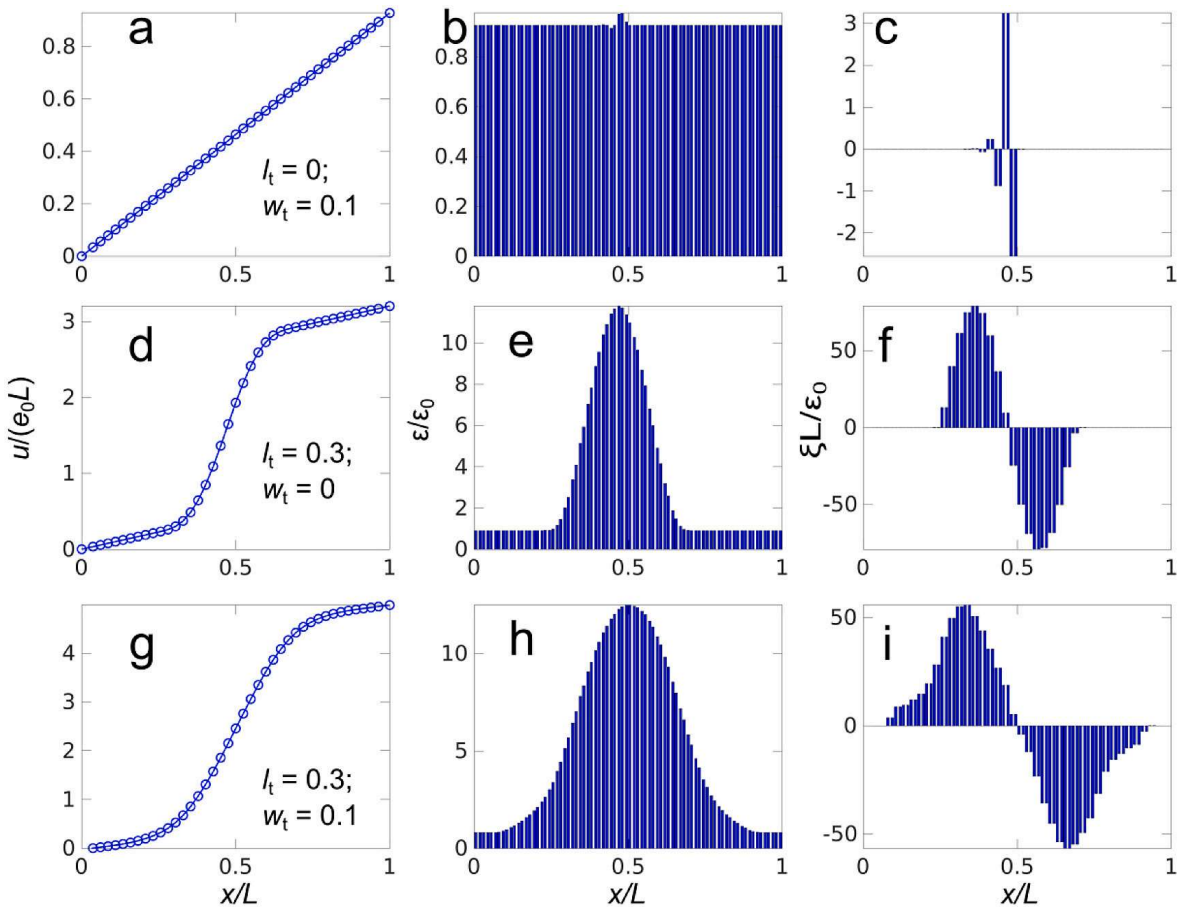

Fig. Appendix-2. (a) For $w_t > 0$ and $l_t = 0$, no equilibrium solution can be found after the damage arises, leading to the oscillation of the iterative solution; b-(c) The effect of non-zero w_t on the enhanced distribution of strain and sprain deformations in a 1D bar subjected to uniaxial tension.

constitutive form, there does not exist a convergent solution for this problem. In fact, the iteration will diverge or the adaptive time step will reduce to an infinitesimal value.

(b) $l_t > 0, w_t > 0$

To resolve the above-mentioned problem, a non-zero w_t needs to be used with non-zero l_t. Figs. Appendix-2g–i show that w_t has a spreading effect on both the strain and sprain deformation profiles compared with the case where only l_t is used (Figs. Appendix-2d–f). Also, the profiles in Figs. Appendix-2h–i exhibited a more gradual reduction of the strain and sprain deformations at the boundary of the regularizing length.

Appendix F. Derivation of w_{char} from the exact solution of a 1D bar

In 1D, a closed-form solution satisfying Eqs. (22)–(24) and the boundary conditions in Eq. (93) is feasible. For the elastic bar, rewriting the equilibrium of stress gives:

$$\frac{\mathrm{d}\sigma}{\mathrm{d}x} = 0 \tag{127}$$

The constitutive relation is:

$$\sigma = E\varepsilon \tag{128}$$

So, the governing equation becomes:

$$\frac{\mathrm{d}\varepsilon}{\mathrm{d}x} = 0 \rightarrow \varepsilon = \text{const.} \rightarrow u = \bar{u}x/L \tag{129}$$

However, when a crack is initiated at the mid-length, i.e. $x = L/2$, a slight modification is necessary. We introduce a source term in Eq. (129) to represent the strain burst, i.e.,

$$\varepsilon(x) = \frac{\mathrm{d}u}{\mathrm{d}x} = \bar{u}\delta(x - L/2) \tag{130}$$

where δ is the Dirac–delta function. The form of the source term function makes sure the second boundary condition in Eq. (93) is satisfied, so that only the first boundary condition needs to be satisfied. This leads to the solution $u = \bar{u}\mathcal{H}(x - L/2)$, where $\mathcal{H}$ is the Heaviside function. It should be noted that the constitutive relation in Eq. (129) must be satisfied everywhere in the bar except for $x = L/2$, so that the stress in the bar would vanish (i.e., the bar gets completely unloaded).

When the higher-order term appears, we apply the same strategy as for the non-local governing equation. For the elastic bar:

$$\frac{\mathrm{d}\sigma}{\mathrm{d}x} - \frac{\mathrm{d}^2\tau}{\mathrm{d}x^2} = 0 \rightarrow \sigma - \frac{\mathrm{d}\tau}{\mathrm{d}x} = \text{const.} \rightarrow \frac{\mathrm{d}u}{\mathrm{d}x} - \frac{\mathrm{d}}{\mathrm{d}x}\left(\frac{l_t^2}{12}\frac{\mathrm{d}^2u}{\mathrm{d}x^2}\right) = \text{const.} \tag{131}$$

Similarly, for the damaged bar, a Dirac delta source term will appear, i.e.,

$$\frac{\mathrm{d}u}{\mathrm{d}x} - \frac{\mathrm{d}}{\mathrm{d}x}\left(\frac{l_t^2}{12}\frac{\mathrm{d}^2u}{\mathrm{d}x^2}\right) = \bar{u}\delta(x - L/2) \rightarrow \frac{\mathrm{d}u}{\mathrm{d}x} - \frac{l_t^2}{12}\frac{\mathrm{d}^3u}{\mathrm{d}x^3} = \bar{u}\delta(x - L/2) \tag{132}$$

As the damage does not occur at the boundary, we can rewrite the boundary condition (24) as:

$$\tau(0) = \tau(L) = 0 \;\rightarrow\; \frac{El_t^2}{12}\frac{\mathrm{d}^2u}{\mathrm{d}x^2}(x = 0 \text{ or } x = L) = 0 \tag{133}$$

Therefore, only three boundary conditions remain, i.e., $u(0) = \mathrm{d}^2u/\mathrm{d}x^2(0) = \mathrm{d}^2u/\mathrm{d}x^2(L) = 0$.

The solution of Eq. (132) is:

$$u = C_1 \exp\left(-\frac{2\sqrt{3}}{l_t}x\right) + C_2 \exp\left(\frac{2\sqrt{3}}{l_t}x\right) + u_p(x) \tag{134}$$

where u_p is the particular solution.

$$\begin{aligned} u_p = {} & \frac{\bar{u}}{2}\exp\left(-\frac{2\sqrt{3}}{l_t}x\right)\left[\mathcal{H}\left(x - \frac{L}{2}\right)\exp\left(\frac{2\sqrt{3}}{l_t}x\right) + \mathcal{H}\left(\frac{L}{2} - x\right)\exp\left(\frac{\sqrt{3}L}{l_t}\right)\right] \\ & + \frac{\bar{u}}{2}\exp\left(\frac{2\sqrt{3}}{l_t}x\right)\left[\mathcal{H}\left(x - \frac{L}{2}\right)\exp\left(-\frac{2\sqrt{3}}{l_t}x\right) + \mathcal{H}\left(\frac{L}{2} - x\right)\exp\left(\frac{-\sqrt{3}L}{l_t}\right)\right] \end{aligned} \tag{135}$$

and,

$$C_1 = -\bar{u}\frac{\cosh\left(\sqrt{3}L/l_t\right)}{1 - \exp\left(-4\sqrt{3}L/l_t\right)}; C_2 = \bar{u}\frac{\cosh\left(\sqrt{3}L/l_t\right)}{\exp\left(4\sqrt{3}L/l_t\right) - 1} \tag{136}$$

The analytically calculated displacement giving the strain and sprain deformation fields of the analytical solution is plotted in Fig. Appendix-3. Note that the strain field in Figs. Appendix-3e, f is concave rather than convex, due to the exponential shape. This is the result of the discontinuous ξ at $x = L/2$, shown in Figs. Appendix-3h, i.

Now we define $\Delta x_{C\%}$ as the distance at which the strain value reaches $C\%$ of the maximum strain (ϵ_{max}; see Fig. Appendix-3f).

$$\epsilon_{max} = \frac{\sqrt{3}\bar{u}}{l_t}\left[\frac{1 + \exp\left(-2\sqrt{3}L/l_t\right)}{1 - \exp\left(-4\sqrt{3}L/l_t\right)} + \frac{\exp\left(2\sqrt{3}L/l_t\right) + 1}{\exp\left(4\sqrt{3}L/l_t\right) - 1}\right] \tag{137}$$

$\epsilon = 0.5\epsilon_{max}$ at $\Delta x_{50\%} \approx 0.45l_t$ and $\epsilon = 0.1\epsilon_{max}$ at $\Delta x_{10\%} \approx 1.32l_t$. The latter can be taken as characteristic width w_{char}. In reality, this value may also depend on E and E_t, which are the Young modulus and the initial softening slope of the constitutive law. The distance should converge to $1.32l_t$ as $E_t \rightarrow \infty$. We may then propose a power-law dependence in Eq. (94), which is confirmed by Fig. Appendix-4.

Appendix G. Further details of the analytical solution of the 1D bar

The second-order derivative of the particular solution, Eq. (135), reads:

$$\begin{aligned} \frac{\mathrm{d}^2u_p}{\mathrm{d}x^2} = \frac{6\bar{u}}{l_t^2}\Bigg\{ & \exp\left(-\frac{2\sqrt{3}}{l_t}x\right)\left[\mathcal{H}\left(x - \frac{L}{2}\right)\exp\left(\frac{2\sqrt{3}}{l_t}x\right) + \mathcal{H}\left(\frac{L}{2} - x\right)\exp\left(\frac{\sqrt{3}L}{l_t}\right)\right] + \\ & \exp\left(\frac{2\sqrt{3}}{l_t}x\right)\left[\mathcal{H}\left(x - \frac{L}{2}\right)\exp\left(-\frac{2\sqrt{3}}{l_t}x\right) + \mathcal{H}\left(\frac{L}{2} - x\right)\exp\left(\frac{-\sqrt{3}L}{l_t}\right)\right] - \\ & 2\mathcal{H}\left(x - \frac{L}{2}\right)\Bigg\} \end{aligned} \tag{138}$$

From the boundary conditions $u(0) = \mathrm{d}^2u/\mathrm{d}x^2(0) = 0$, we have

$$C_1 + C_2 = -\bar{u}\cosh\left(\frac{\sqrt{3}L}{l_t}\right) \tag{139}$$

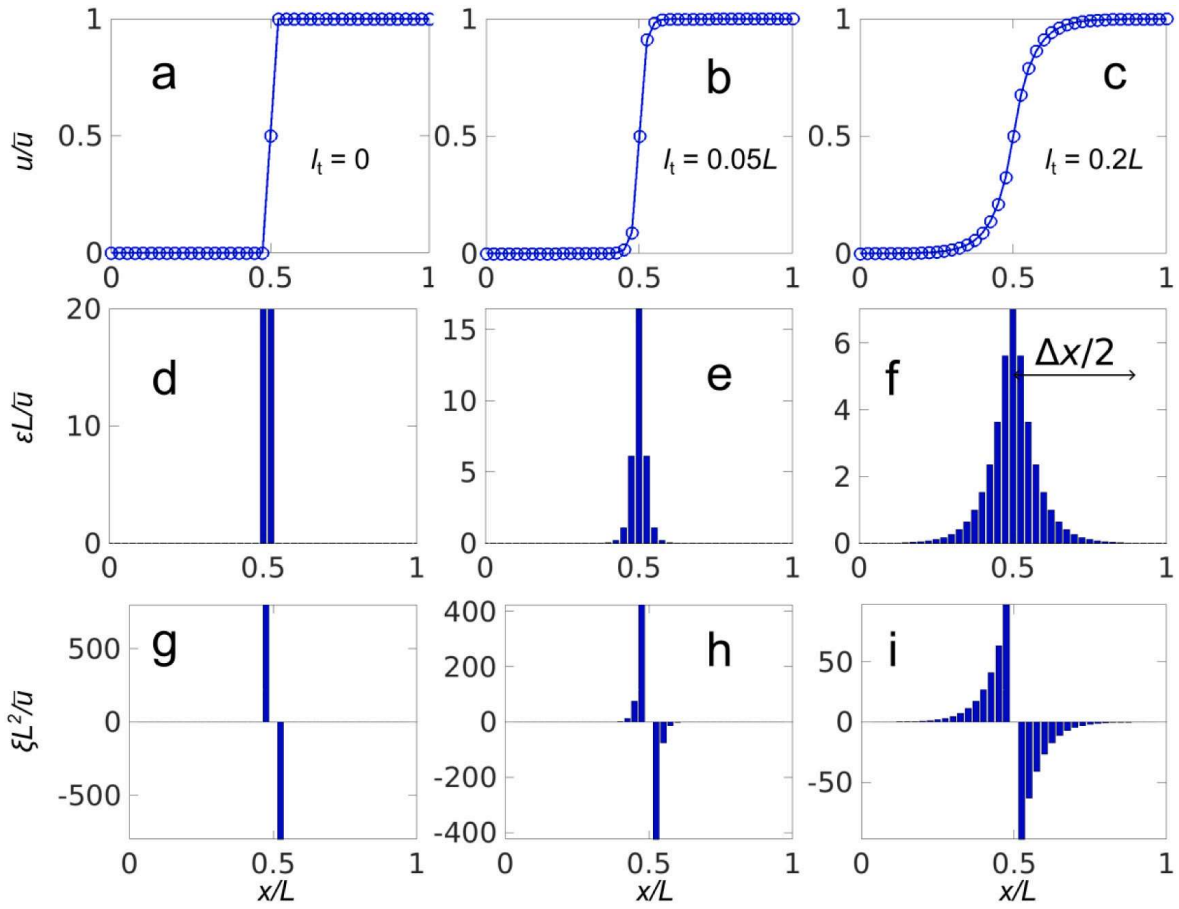

Fig. Appendix-3. Analytical solutions of the normalized displacement (a–c), strain (d–f), and sprain deformation (g–i) of a 1D bar subjected to uniaxial tension (with $l_t = 0; 0.05L; 0.2L$). Note that, the ε and ξ value at $x = L/2$ were computed using the central difference approximation of the displacement field.

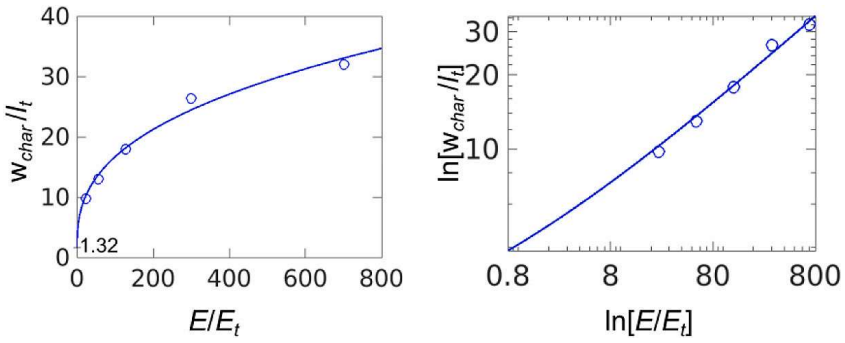

Fig. Appendix-4. The material characteristic size w_{char} as a function of the regularizing length l_t and E/E_t. Note that in the natural log–log scale this function asymptotically converges to a straight line as $E/E_t \to \infty$, suggesting a power-law function.

On the other hand, from $\mathrm{d}^2u/\mathrm{d}x^2(L) = 0$ we obtain:

$$C_2 = -C_1 \exp\left(\frac{-4\sqrt{3}L}{l_t}\right) \tag{140}$$

Solving these two Eqs., we obtain C_1, C_2 in Eqs. (136)

The first derivative of the analytical solution is:

$$\frac{\mathrm{d}u}{\mathrm{d}x} = -\frac{2\sqrt{3}}{l_t} C_1 \exp\left(\frac{-2\sqrt{3}}{l_t}x\right) + \frac{2\sqrt{3}}{l_t} C_2 \exp\left(\frac{2\sqrt{3}}{l_t}x\right) + \frac{\mathrm{d}u_p}{\mathrm{d}x} \tag{141}$$

where

$$\frac{\mathrm{d}u_p}{\mathrm{d}x} = \frac{\sqrt{3}\bar{u}}{l_t}\left\{ -\exp\left(-\frac{2\sqrt{3}}{l_t}x\right)\left[\mathcal{H}\left(x-\frac{L}{2}\right)\exp\left(\frac{2\sqrt{3}}{l_t}x\right)+\mathcal{H}\left(\frac{L}{2}-x\right)\exp\left(\frac{\sqrt{3}L}{l_t}\right)\right]\right.$$
$$\left.+\exp\left(\frac{2\sqrt{3}}{l_t}x\right)\left[\mathcal{H}\left(x-\frac{L}{2}\right)\exp\left(-\frac{2\sqrt{3}}{l_t}x\right)+\mathcal{H}\left(\frac{L}{2}-x\right)\exp\left(\frac{-\sqrt{3}L}{l_t}\right)\right]\right\} \tag{142}$$

Note that:

$$\varepsilon = \frac{\mathrm{d}u_p}{\mathrm{d}x}\left(x>\frac{L}{2}\right)=0 \tag{143}$$

Appendix H. Broader context

The finite dimension of fracture process zone and its consequence

Quasibrittle materials are materials in which the fracture process zone (FPZ) has a finite length and, importantly, also a finite width. This feature, a consequence of material heterogeneity, is what limits localization of material damage (Bažant and Kazemi, 1990). In (perfectly) brittle materials this is not the case at normal scales of application. However, on sufficiently small scale every brittle material becomes quasibrittle, while at sufficiently large every material can be treated as brittle, although this is frequently beyond practical reach. The heterogeneity can be due to inclusions or patches of different properties, to weak interfaces, or to the deepest nano-structure as in polymers where the crazing is due to the length of macromolecular chains. In concrete, the archetypical quasibrittle material, it is the mineral aggregate size that limits damage localization at fracture front, before damage can coalesce into rough continuous crack (Bažant and Planas, 1998). Other materials that are quasibrittle at normal scale of usage are fiber-reinforced concrete, sea ice, tough ceramics, fiber composites, stiff foams, many rocks, wood, carton, bones, biological shells, etc.

A classical way to capture quasibrittleness has been the cohesive crack model, conceived in 1958 by G.I. Barenblatt (Barenblatt, 1959, 1962) (for errors in history see Chorin and Bažant, 2022). However, the gap tests (Nguyen et al., 2020a,b) showed in 2020 that the assumption of a line crack with a scalar stress-separation relation was valid only if the crack-parallel stresses were negligible, which is rare in practice. The gap test demonstrated that not only the length but also the finite width of a fracture process zone (FPZ) governed the fracture behavior. Hence, for a numerical method to adequately describe the fracture behavior, a tensorial damage constitutive law must be formulated to capture the evolution of the FPZ.

In recent decades, the study of nano-to-microscale behavior has shed more light on its effect on the macroscale fracture behavior of materials. Several studies (Zhang et al., 2021; Yang et al., 2021; Zhang et al., 2022) showed that materials seemingly brittle at the macroscale (Yang et al., 2017) normally exhibit inelastic zones of nanometer size, due to nanoscale inhomogeneity. This makes them quasi-brittle at that scale.

The fracture of plastic-hardening metals is more complicated because the softening damage in the FPZ is not surrounded by an elastic zone but by a yielding zone, causing that two length scales, characterizing the widths of crack front and of yielding zone, intervene (Nguyen et al., 2021b; Dönmez et al., 2023). These length scales characterize the dislocation pile-ups and void coalescence at the crack front and are functions of the size of the polycrystal grains. For example, dislocations tend to migrate, accumulate and form micro-voids at the grain boundaries due to the lower energy barrier. These micro-voids then coalesce and result in a major crack. Therefore, the size (and shape) of the crystal grains affect the yielding and fracture resistance of these metals. The plastic yielding and fracture of these materials are there governed by zones with finite dimensions (Hancock et al., 1993; Gao et al., 1996; Yuan and Brocks, 1998; Zhu and Leis, 2006; Liu et al., 2019). However, in other cases, dislocation arrest at crack boundaries explains the Hall–Petch effect of grain size on the yield strength and hardening slope of metals (Hall, 1951). (However, one needs to see that yet Hall–Petch effect is a material size effect which must not be confused with the structural size effect (crystal size versus structure size).) For these reasons, the cracks in polycrystalline metals are not line cracks, as typically considered, but have an FPZ of finite width, about 5 μm, which suffices to cause a strong dependence of fracture energy on the crack-parallel stress (Dönmez et al., 2023).

The crack front width in polycrystalline metals and the transition from large-scale to small-scale yielding were recently shown to require a generalization of size effect law in which the large-scale yielding causes the size effect to exhibit intermediate asymptote (in the sense of Barenblatt, 1996, 2014). The use of this asymptote enables an alternative method for determining the J-integral by size effect tests of relatively small size. The microscale width of the front of a crack within the yielding zone of polycrystalline metal causes the fracture energy (or J-integral) to depend on the crack-parallel stresses (or T-stress). As a result, the crack front constraint caused by plasticity within a yielding zone (YZ) at the crack front would alter the fracture energy of the material (in a way similar to the $J-Q$ or $J-T$ constraint). The scaling law for the transition from large-scale to small-scale yielding (Dönmez et al., 2023) and the associated crack-parallel stress effect should be a basic check for developing computational a model of fracture of polycrystalline metals.

The presence of the finite-size FPZ at other materials is evidenced by their effect on semiconducting 2D materials, reinforced concrete, fiber composites, bone, sea ice, etc.; e.g. Yang et al. (2021), Zhang et al. (2022) and Brockmann and Salviato (2023).

Table 2
Pros and Cons of some common strain-regularization methods.

Method	Pros	Cons
Gradient damage	• The results are consistent regardless of mesh size • Ensures delta-convergence of a smearing length scale	• A well-established constitutive law is difficult to implement • Length scale interpretation for quasi-brittle and ductile damage is ambiguous • Resistance to the gradient of material rotation tensor is ignored • Boundary conditions are nonphysical, and on the crack surfaces near the tip particularly harmful • Convergence often requires extremely fine mesh along the crack path and local mesh refinement. • Experiences stress-locking (Jirásek and Zimmermann, 1998; Zhang et al., 2015; Wu et al., 2020)
Strain-gradient	• Can be used with any constitutive law • The results are consistent regardless of the mesh	• One extra degree of freedom is needed, which increases the computational cost in data storage and linear system solver • Need for additional essential boundary conditions, which have no physical basis, particularly deleterious on crack surfaces near crack front • Resistance to the gradient of material rotation tensor derived from the displacement field is ignored
Integral-type nonlocal damage	• Can be used with any constitutive law • Nonlocal strain is easy to compute	• Results depend on the attenuation function • Storage of nodal solutions and state variables must be shared across processors presenting challenges to efficient parallelization • The necessary adjustment of boundary conditions is nonphysical and particularly deleterious on the crack surfaces near the tip • Often problematic for damage zones near the domain boundary
Viscous regularization	• Can be used with any constitutive law • Improves "well-posedness" of the problem and nonlinear convergence	• Damage develops too slow or too fast if the viscosity is not right, and gives realistic results for only one loading rate unknown a priori • Adds a bias to the unloading process and load cycling • Does not predict a spatially constant fracture energy and gives distorted results due to locally nonuniform loading rates (Langenfeld et al., 2022).

Higher-order continuum theory

Material rotations were also used in other models. For example they appear in Cosserat and micropolar-based continuum approaches (Cosserat and Cosserat, 1909; Eringen, 2012), but in a different context—continuum smoothing of elastic materials with microstructure. These rotations represent independent degrees of freedom and not derivatives of the displacement field. The purpose is, e.g., to distinguish the rotations of joints from rotations of beams in an elastic framework (Cedolin et al., 2010, chapter 2), or to represent the rotations of grains in a shear or compaction band of granular material. As another example, Placidi et al. (2018, 2022a,b) considered gradient regularization in a variational framework, yet the choice of the energy function was arbitrary and not reflecting material heterogeneity effect.

To capture numerically the size and shape effects of the inelastic zones and the corresponding energy that they release or dissipate, several methods have been proposed. For YZ, strain-gradient plasticity theory using the gradients of the strain field to limit the dislocation density in a certain volume of metal (Hutchinson and Fleck, 1997; Gurtin and Anand, 2005a,b) was used to capture the microscale physics of the yielding process. However, the small-size asymptotic behavior was shown to exhibit power-law scaling of unreasonably large exponent (Bažant, 2002).

For fracture and damage due to the localizing tendency of softening material points, a few regularization methods have been proposed to accompany physically sound constitutive laws. These methods include, but are not limited to, partial regularization techniques (a widely used example is the crack-band theory (Bažant and Oh, 1983)), gradient damage methods (among them is the notable phase-field method (Marigo, 1989; Pham et al., 2011; Miehe et al., 2016)), strain-gradient methods (Peerlings et al., 1996), integral-type nonlocal damage methods (Pijaudier-Cabot and Bažant, 1987; Bažant, 1994), or regularization methods based on real or artificial viscosity (Ladeveze, 1992, 1995; Ladevèze et al., 2000). The relative strengths and weaknesses of these approaches have been discussed in the literature and are summarized in Table 2.

Similar localization limiters were also used for crystalline metals. In single-crystal metals, the flow strength depends on the statistically stored and geometrically necessary dislocation densities (Ashby, 1970; Russell and Ashby, 1970), which, in turn, are functions of the local variation of the deformation field. This observation gave rise to strain-gradient plasticity theory (Hutchinson and Fleck, 1997) which, however did not perform very well. It was soon replaced by the (very successful) mechanism-based strain-gradient plasticity (Gao et al., 1999) in which, as already mentioned, the strain gradient tensor enters only through its invariants, as scalar parameters in a regular hardening plasticity model. The necessity of this revision was also identified in Bažant (2002) by showing unrealistically strong asymptotic size effect of the strain gradient theory.

References

Alaydin, M.D., Benson, D.J., Bazilevs, Y., 2021. An updated Lagrangian framework for isogeometric Kirchhoff–Love thin-shell analysis. Comput. Methods Appl. Mech. Engrg. 384, 113977.

Ashby, M.F., 1970. The deformation of plastically non-homogeneous materials. Phil. Mag. A 21 (170), 399–424.

Barenblatt, G.I., 1959. The formation of equilibrium cracks during brittle fracture. General ideas and hypotheses. Axially-symmetric cracks. J. Appl. Math. Mech. 23 (3), 622–636.

Barenblatt, G.I., 1962. The mathematical theory of equilibrium cracks in brittle fracture. Adv. Appl. Mech. 7, 55–129.

Barenblatt, G.I., 1996. Scaling, Self-Similarity, and Intermediate Asymptotics: Dimensional Analysis and Intermediate Asymptotics. In: Cambridge Texts in Applied Mathematics, Cambridge University Press, http://dx.doi.org/10.1017/CBO9781107050242.

Barenblatt, G.I., 2014. Flow, Deformation and Fracture: Lectures on Fluid Mechanics and the Mechanics of Deformable Solids for Mathematicians and Physicists, vol. 49. Cambridge University Press.

Batdorf, S.B., Budiansky, B., 1949. A Mathematical Theory of Plasticity Based on the Concept of Slip. Tech. Rep., National Advisory Committee for Aeronautics.

Bažant, Z.P., 1984. Imbricate continuum and its variational derivation. J. Eng. Mech. 110 (12), 1693–1712.

Bažant, Z.P., 1994. Nonlocal damage theory based on micromechanics of crack interactions. J. Eng. Mech. 120 (3), 593–617.

Bažant, Z.P., 2002. Scaling of dislocation-based strain-gradient plasticity. J. Mech. Phys. Solids 50 (3), 435–448.

Bažant, Z.P., Adley, M.D., Carol, I., Jirásek, M., Akers, S.A., Rohani, B., Cargile, J.D., Caner, F.C., 2000. Large-strain generalization of microplane model for concrete and application. J. Eng. Mech. 126 (9), 971–980.

Bažant, Z.P., Kazemi, M.T., 1990. Size effect in fracture of ceramics and its use to determine fracture energy and effective process zone length. J. Am. Ceram. Soc. 73 (7), 1841–1853.

Bažant, Z.P., Le, J.-L., Salviato, M., 2021. Quasibrittle Fracture Mechanics and Size Effect: A First Course. Oxford University Press.

Bažant, Z.P., Nguyen, H.T., 2023. Proposal of m-index for rating fracture and damage models by their ability to represent a set of distinctive experiments. J. Eng. Mech. 149 (8), 04023047.

Bažant, Z.P., Nguyen, H.T., Abdullah Dönmez, A., 2022. Critical comparison of phase-field, peridynamics, and crack band model M7 in light of gap test and classical fracture tests. J. Appl. Mech. 89 (6), 061008.

Bažant, Z.P., Oh, B.H., 1983. Crack band theory for fracture of concrete. Mater. Struct. 16, 155–177.

Bažant, Z.P., Oh, B.H., 1985. Microplane model for progressive fracture of concrete and rock. J. Eng. Mech. 111 (4), 559–582.

Bažant, P., Oh, B., 1986. Efficient numerical integration on the surface of a sphere. ZAMM Z. Angew. Math. Mech. 66 (1), 37–49.

Bažant, Z.P., Planas, J., 1998. Fracture and Size Effect in Concrete and Other Quasibrittle Materials. CRC Press.

Bažant, Z.P., Prat, P.C., 1988. Microplane model for brittle-plastic material: I. Theory. J. Eng. Mech. 114 (10), 1672–1688.

Belytschko, T., Liu, W.K., Moran, B., Elkhodary, K., 2014. Nonlinear Finite Elements for Continua and Structures. John wiley & sons.

Brocca, M., Bažant, Z.P., 2000. Microplane constitutive model and metal plasticity. Appl. Mech. Rev. 53 (10), 265–281.

Brockmann, J., Salviato, M., 2023. The gap test–effects of crack parallel compression on fracture in carbon fiber composites. Composites A 164, 107252.

Budiansky, B., 1959. A reassessment of deformation theories of plasticity. J. Appl. Mech. 26, 259–264.

Caner, F.C., Bažant, Z.P., 2013a. Microplane model M7 for plain concrete. I: Formulation. J. Eng. Mech. 139 (12), 1714–1723.

Caner, F.C., Bažant, Z.P., 2013b. Microplane model M7 for plain concrete. II: Calibration and verification. J. Eng. Mech. 139 (12), 1724–1735.

Caner, F.C., Bažant, Z.P., Červenka, J., 2002. Vertex effect in strain-softening concrete at rotating principal axes. J. Eng. Mech. 128 (1), 24–33.

Carol, I., Bazant, Z.P., 1997. Damage and plasticity in microplane theory. Int. J. Solids Struct. 34 (29), 3807–3835.

Carol, I., Bažant, Z.P., Prat, P.C., 1991. Geometric damage tensor based on microplane model. J. Eng. Mech. 117 (10), 2429–2448.

Cedolin, L., et al., 2010. Stability of Structures: Elastic, Inelastic, Fracture and Damage Theories. World Scientific.

Chorin, A.J., Bažant, Z.P., 2022. Grigory isaakovich barenblatt. 10 July 1927–22 June 2018.

Clough, R.W., 1960. The finite element method in plane stress analysis. In: Proc., 2nd ASCE Conf. on Electronic Computation. Pittsburgh, PA.

Clough, R.W., 1962. The stress distribution of norfork dam. In: Structures and Materials Series 100, IER 19, Civ. Eng. Dept., U.Cal. Berkeley. Contract DA-03-050-Civeng-62-511, U.S. Army Eng.D. Little Rock, Institute of Engineering Research, Final Report to the Corps of Engineers, p. 134.

Clough, R.W., Wilson, E.L., 1962. Stress analysis of a gravity dam by the finite element method. In: Proceedings, Symposium on the Use of Computers in Civil Engineering. Laboratório Nacional de Engenharia Civil, Lisbon, Portugal, Pittsburgh, PA, pp. 29.1–29.22.

Cosserat, E.M.P., Cosserat, F., 1909. Théorie des Corps Déformables. A. Hermann et fils.

Cottrell, J.A., Hughes, T.J.R., Bazilevs, Y., 2009. Isogeometric Analysis: Toward Integration of CAD and FEA. John Wiley & Sons.

Dönmez, A.A., Nguyen, H.T., Xu, H., Bažant, Z.P., 2023. Crack-parallel stress effect on fracture energy of plastic hardening polycrystalline metal identified from gap test scaling. J. Mech. Phys. Solids 173, 105222.

Eringen, A.C., 2012. Microcontinuum Field Theories: I. Foundations and Solids. Springer Science & Business Media.

Gao, H., Huang, Y., Nix, W.D., Hutchinson, J.W., 1999. Mechanism-based strain gradient plasticity—I. Theory. J. Mech. Phys. Solids 47 (6), 1239–1263.

Gao, X., Shih, C., Tvergaard, V., Needleman, A., 1996. Constraint effects on the ductile-brittle transition in small scale yielding. J. Mech. Phys. Solids (ISSN: 0022-5096) 44 (8), 1255–1282.

Geel, van, H.J.G.M., 1995. Behaviour of Concrete in Plane Strain Compression: Influence of Stress Path and Specimen Size. TU Eindhoven. Fac. Bouwkunde, Vakgr. Konstruktie, Technische Universiteit Eindhoven.

Gerard, G., Becker, H., 1957. Handbook of Structural Stability: part I, Buckling of Flat Plates, NACA Tech. Tech. Rep., Note.

Grégoire, D., Rojas-Solano, L.B., Pijaudier-Cabot, G., 2013. Failure and size effect for notched and unnotched concrete beams. Int. J. Numer. Anal. Methods Geomech. 37 (10), 1434–1452.

Gurtin, M.E., Anand, L., 2005a. A theory of strain-gradient plasticity for isotropic, plastically irrotational materials. Part I: Small deformations. J. Mech. Phys. Solids 53 (7), 1624–1649.

Gurtin, M.E., Anand, L., 2005b. A theory of strain-gradient plasticity for isotropic, plastically irrotational materials. Part II: Finite deformations. Int. J. Plast. 21 (12), 2297–2318.

Hall, E.O., 1951. The deformation and ageing of mild steel: III discussion of results. Proc. Phys. Soc. B 64 (9), 747.

Hancock, J.W., Reuter, W.G., Parks, D.M., 1993. Constraint and toughness parameterized by T. ASTM Special Tech. Publ. 1171, 21.

Hoover, C.G., Bažant, Z.P., 2014. Cohesive crack, size effect, crack band and work-of-fracture models compared to comprehensive concrete fracture tests. Int. J. Fract. 187 (1), 133–143.

Hughes, T.J.R., 2012. The Finite Element Method: Linear Static and Dynamic Finite Element Analysis. Courier Corporation.

Hughes, T.J.R., Cottrell, J.A., Bazilevs, Y., 2005. Isogeometric analysis: CAD, finite elements, NURBS, exact geometry and mesh refinement. Comput. Methods Appl. Mech. Engrg. 194 (39–41), 4135–4195.

Hughes, T.J.R., Feijóo, G.R., Mazzei, L., Quincy, J.-B., 1998. The variational multiscale method—A paradigm for computational mechanics. Comput. Methods Appl. Mech. Engrg. 166 (1–2), 3–24.

Hutchinson, J., Fleck, N., 1997. Strain gradient plasticity. Adv. Appl. Mech. 33, 295–361.

Jirásek, M., Bažant, Z.P., 2001. Inelastic Analysis of Structures. John Wiley & Sons.

Jirásek, M., Zimmermann, T., 1998. Analysis of rotating crack model. J. Eng. Mech. 124 (8), 842–851.

Johnson, G.R., Peterson, E.H., Schonhardt, J.A., Stryk, R.A., Holmquist, T.J., Burns, C.R., 1996. User Instructions for the Final Version of the EPIC Research Code. Tech. Rep., Alliant Techsystems Inc Brooklyn Park, MN.
Kirane, K., Bažant, Z.P., 2015. Microplane damage model for fatigue of quasibrittle materials: Sub-critical crack growth, lifetime and residual strength. Int. J. Fatigue 70, 93–105.
Ladeveze, P., 1992. A damage computational method for composite structures. Comput. Struct. 44 (1–2), 79–87.
Ladeveze, P., 1995. A damage computational approach for composites: Basic aspects and micromechanical relations. Comput. Mech. 17 (1–2), 142–150.
Ladevèze, P., Allix, O., Deü, J.-F., Lévêque, D., 2000. A mesomodel for localisation and damage computation in laminates. Comput. Methods Appl. Mech. Engrg. 183 (1–2), 105–122.
Lale, E., Cusatis, G., 2021. Symmetric high order microplane model for damage localization and size effect in quasi-brittle materials. Int. J. Numer. Anal. Methods Geomech. 45 (10), 1458–1476.
Lale, E., Zhou, X., Cusatis, G., 2017. Isogeometric implementation of high-order microplane model for the simulation of high-order elasticity, softening, and localization. J. Appl. Mech. 84 (1).
Langenfeld, K., Kurzeja, P., Mosler, J., 2022. How regularization concepts interfere with quasibrittle damage: A comparison based on a unified variational framework. Contin. Mech. Thermodyn. 34 (6), 1517–1544.
Li, W., Bazilevs, Y., 2023. An improved formulation for reduced quadrature in computational solid mechanics. Comput. Mech. 1–12.
Li, W., Moutsanidis, G., Behzadinasab, M., Hillman, M., Bazilevs, Y., 2022. Reduced quadrature for finite element and isogeometric methods in nonlinear solids. Comput. Methods Appl. Mech. Engrg. 399, 115389.
Liu, Z., Wang, X., Tang, J., Deng, C., Zhao, H., Chen, X., 2019. The effects of in-plane and out-of-plane constraints on JR curves for X80 steel: A study using clamped SENT specimens. Eng. Fract. Mech. 206, 342–358.
Marigo, J.-J., 1989. Constitutive relations in plasticity, damage and fracture mechanics based on a work property. Nucl. Eng. Des. 114 (3), 249–272.
Mazars, J., 1984. Application de la Mécanique de L'Endommagement Au Comportement Non Linéaire et à la Rupture Du Béton de Structure (Ph.D. thesis). Université Paris 6, France.
Miehe, C., Aldakheel, F., Raina, A., 2016. Phase field modeling of ductile fracture at finite strains: A variational gradient-extended plasticity-damage theory. Int. J. Plast. 84, 1–32.
Monchiet, V., Bonnet, G., 2011. Inversion of higher order isotropic tensors with minor symmetries and solution of higher order heterogeneity problems. Proc. R. Soc. A 467 (2126), 314–332.
Nguyen, H.T., Caner, F.C., Bažant, Z.P., 2021a. Conversion of explicit microplane model with boundaries to a constitutive subroutine for implicit finite element programs. Internat. J. Numer. Methods Engrg. 122 (6), 1563–1577.
Nguyen, H.T., Dönmez, A.A., Bažant, Z.P., 2021b. Structural strength scaling law for fracture of plastic-hardening metals and testing of fracture properties. Extreme Mech. Lett. 43, 101141.
Nguyen, H.T., Pathirage, M., Cusatis, G., Bažant, Z.P., 2020a. Gap test of crack-parallel stress effect on quasibrittle fracture and its consequences. J. Appl. Mech. 87 (7), 071012.
Nguyen, H., Pathirage, M., Rezaei, M., Issa, M., Cusatis, G., Bažant, Z.P., 2020b. New perspective of fracture mechanics inspired by gap test with crack-parallel compression. Proc. Natl. Acad. Sci. 117 (25), 14015–14020.
Ožbolt, J., Gambarelli, S., 2018. Microplane model with relaxed kinematic constraint in the framework of micro polar Cosserat continuum. Eng. Fract. Mech. 199, 476–488.
Peerlings, R.H.J., de Borst, R., Brekelmans, W.A.M., de Vree, J., 1996. Gradient enhanced damage for quasi-brittle materials. Int. J. Numer. Methods Eng. 39 (19), 3391–3403.
Pham, K., Amor, H., Marigo, J.-J., Maurini, C., 2011. Gradient damage models and their use to approximate brittle fracture. Int. J. Damage Mech. 20 (4), 618–652.
Pigazzini, M.S., Bazilevs, Y., Ellison, A., Kim, H., 2018. Isogeometric analysis for simulation of progressive damage in composite laminates. J. Compos. Mater. 52 (25), 3471–3489.
Pijaudier-Cabot, G., Bažant, Z.P., 1987. Nonlocal damage theory. J. Eng. Mech. 113 (10), 1512–1533.
Pijaudier-Cabot, G., Mazars, J., 2001. Damage models for concrete. In: Lemaitre, J. (Ed.), Handbook of Materials Behavior Models. Academic Press, p. 1232.
Placidi, L., Barchiesi, E., Dell'Isola, F., Maksimov, V., Misra, A., Rezaei, N., Scrofani, A., Timofeev, D., 2022a. On a hemi-variational formulation for a 2D elasto-plastic-damage strain gradient solid with granular microstructure. Math. Eng. 5, 1–24.
Placidi, L., Barchiesi, E., Misra, A., 2018. A strain gradient variational approach to damage: A comparison with damage gradient models and numerical results. Math. Mech. Complex Syst. 6 (2), 77–100.
Placidi, L., Timofeev, D., Maksimov, V., Barchiesi, E., Ciallella, A., Misra, A., dell'Isola, F., 2022b. Micro-mechano-morphology-informed continuum damage modeling with intrinsic 2nd gradient (pantographic) grain–grain interactions. Int. J. Solids Struct. 254, 111880.
Rice, J.R., 2006. Heating and weakening of faults during earthquake slip. J. Geophys. Res. Solid Earth 111 (B5).
Russell, K.G., Ashby, M.F., 1970. Slip in aluminum crystals containing strong, plate-like particles. Acta Metall. 18 (8), 891–901.
Stroud, A.H., 1971. Approximate Calculation of Multiple Integrals. Prentice-Hall.
Taylor, L.M., Flanagan, D.P., 1989. PRONTO 3D: a Three-Dimensional Transient Solid Dynamics Program. Tech. Rep., Sandia National Lab. (SNL-NM), Albuquerque, NM (United States).
Wang, P., Sang, Y., Shao, L., Guo, X., 2019. Measurement of the deformation of sand in a plane strain compression experiment using incremental digital image correlation. Acta Geotech. 14, 547–557.
Wen, J., Tang, L., Zhang, S., Zhan, Q., Wang, Y., 2023. Qualitative and quantitative investigations on the failure effect of critical fissures in rock specimens under plane strain compression. Materials 16 (2), 611.
Wu, J.-Y., Nguyen, V.P., Zhou, H., Huang, Y., 2020. A variationally consistent phase-field anisotropic damage model for fracture. Comput. Methods Appl. Mech. Engrg. 358, 112629.
Yang, Y., Li, X., Wen, M., Hacopian, E., Chen, W., Gong, Y., Zhang, J., Li, B., Zhou, W., Ajayan, P.M., et al., 2017. Brittle fracture of 2D $MoSe_2$. Adv. Mater. 29 (2), 1604201.
Yang, Y., Song, Z., Lu, G., Zhang, Q., Zhang, B., Ni, B., Wang, C., Li, X., Gu, L., Xie, X., et al., 2021. Intrinsic toughening and stable crack propagation in hexagonal boron nitride. Nature 594 (7861), 57–61.
Yuan, H., Brocks, W., 1998. Quantification of constraint effects in elastic-plastic crack front fields. J. Mech. Phys. Solids 46 (2), 219–241.
Zhang, Y., Bažant, Z.P., 2023. Smooth crack band model—A computational paragon based on unorthodox continuum homogenization. J. Appl. Mech. 90 (4), 041007.
Zhang, Y., Lackner, R., Zeiml, M., Mang, H.A., 2015. Strong discontinuity embedded approach with standard SOS formulation: Element formulation, energy-based crack-tracking strategy, and validations. Comput. Methods Appl. Mech. Engrg. 287, 335–366.
Zhang, X., Nguyen, H., Paci, J.T., Sankaranarayanan, S.K.R.S., Mendoza-Cortes, J.L., Espinosa, H.D., 2021. Multi-objective parametrization of interatomic potentials for large deformation pathways and fracture of two-dimensional materials. NPJ Comput. Mater. 7 (1), 113.
Zhang, X., Nguyen, H., Zhang, X., Ajayan, P.M., Wen, J., Espinosa, H.D., 2022. Atomistic measurement and modeling of intrinsic fracture toughness of two-dimensional materials. Proc. Natl. Acad. Sci. 119 (45), e2206756119.
Zhou, W., Cheng, J., Zhang, G., Li, H., Cheng, Y., Ma, G., Ji, X., 2021. Effects of wetting–drying cycles on the breakage characteristics of slate rock grains. Rock Mech. Rock Eng. 54 (12), 6323–6337.
Zhu, X.-K., Leis, B.N., 2006. Bending modified J–Q theory and crack-tip constraint quantification. Int. J. Fract. 141 (1), 115–134.